


Article

Substitution of Co with Ni in Co/Al₂O₃ Catalysts for Fischer–Tropsch Synthesis

Michela Martinelli ¹, Sai Charan Karuturi ², Richard Garcia ³, Caleb D. Watson ³,
Wilson D. Shafer ⁴ , Donald C. Cronauer ⁵, A. Jeremy Kropf ⁵, Christopher L. Marshall ⁵ and
Gary Jacobs ^{1,3,*}

¹ University of Kentucky Center for Applied Energy Research, 2540 Research Park Drive, Lexington, KY 40511, USA; michela.martinelli@uky.edu

² Department of Mechanical Engineering, University of Texas at San Antonio, One UTSA Circle, San Antonio, TX 78249, USA; saicharan.karuturi@my.utsa.edu

³ Department of Biomedical Engineering and Chemical Engineering, University of Texas at San Antonio, One UTSA Circle, San Antonio, TX 78249, USA; g123richard@gmail.com (R.G.); caleb.watson378@gmail.com (C.D.W.)

⁴ Department of Chemistry, Asbury University, One Macklem Drive, Wilmore, KY 40390, USA; Wilson.Shafer@asbury.edu

⁵ Argonne National Laboratory, Argonne, IL 60439, USA; dccronauer@anl.gov (D.C.C.); kropf@anl.gov (A.J.K.); marshall@anl.gov (C.L.M.)

* Correspondence: garyjacobs@utsa.edu; Tel.: +1-210-458-7080

Received: 22 February 2020; Accepted: 15 March 2020; Published: 17 March 2020



Abstract: The effect of cobalt substitution with nickel was investigated for the Fischer–Tropsch synthesis reaction. Catalysts having different Ni/Co ratios were prepared by aqueous incipient wetness co-impregnation, characterized, and tested using a continuously stirred tank reactor (CSTR) for more than 200 h. The addition of nickel did not significantly modify the morphological properties measured. XRD, STEM, and TPR-XANES results showed intimate contact between nickel and cobalt, strongly suggesting the formation of a Co–Ni solid oxide solution in each case. Moreover, TPR-XANES indicated that nickel addition improves the cobalt reducibility. This may be due to H₂ dissociation and spillover, but is more likely the results of a chemical effect of intimate contact between Co and Ni resulting in Co–Ni alloying after activation. FTS testing revealed a lower initial activity when nickel was added. However, CO conversion continuously increased with time on-stream until a steady-state value (34%–37% depending on Ni/Co ratio) was achieved, which was very close to the value observed for undoped Co/Al₂O₃. This trend suggests nickel can stabilize cobalt nanoparticles even at a lower weight percentage of Co. Currently, the cobalt price is 2.13 times the price of nickel. Thus, comparing the activity/price, the catalyst with a Ni/Co ratio of 25/75 has better performance than the unpromoted catalyst. Finally, nickel-promoted catalysts exhibited slightly higher initial selectivity for light hydrocarbons, but this difference typically diminished with time on-stream; once leveling off in conversion was achieved, the C₅₊ selectivities were similar (≈ 80%) for Ni/Co ratios up to 10/90, and only slightly lower (≈ 77%) at Ni/Co of 25/75.

Keywords: Fischer–Tropsch synthesis; bimetallic catalyst; cobalt–nickel alloys; TPR-XANES/EXAFS

1. Introduction

Fischer–Tropsch synthesis (FTS) is a catalytic reaction which converts syngas, a mixture of CO and H₂ derived from natural gas, coal, and/or biomass, to high quality fuels. The active metals for FTS are iron, cobalt, nickel, and ruthenium. Among these metals, ruthenium is the most active. However, its application for large-scale FTS plants is impractical because of low abundance and very high

cost [1]. In contrast, nickel is cheaper, but high selectivities for short-chained hydrocarbons, especially methane, are obtained, because of its high hydrogenation capability [2]. Thus, cobalt and iron are the only relevant catalysts which are currently used commercially. Cobalt is especially advantageous for converting methane-derived syngas because of its high activity and selectivity for linear long-chained hydrocarbons, low deactivation rate, and finally, low activity for water–gas shift (WGS) [3,4]. However, cobalt is more expensive than iron. Indeed, the price of cobalt in the last five years has been within the range of 22–100 \$/kg [5].

The activity of a cobalt catalyst depends on the number of exposed Co^0 atoms, the active sites, on the catalyst's surface [6]. Systems with relatively high dispersions are needed in order to maximize the surface availability of Co^0 . For this reason, cobalt is typically supported on high surface area carriers with strong interactions (e.g., Al_2O_3 , TiO_2). However, thermodynamic studies suggest cobalt nanoparticles lower than 4 nm might be reoxidized by water under FTS reaction conditions [7,8]. Thus, the optimal particle sizes are in the range of 6–10 nm [9]. Even if the particle size, as well as the interaction with the support, are optimized, the majority of the cobalt is locked within the particle instead of being exposed to the surface. Therefore, the incorporation of a second metal, less expensive and with electronic properties close to that of cobalt, could be a possible route to decreasing the total preparation cost of the catalyst. DFT screening was used by Van Helden et al. [10] to identify the alloys which have similar adsorption and electronic properties to the cobalt catalyst. NiCo_3 , AlNi_3 , and SiFe_3 are suitable cheaper candidates. However, SiFe_3 and AlNi_3 are quite difficult to produce at the nanoscale level. In contrast, Co–Ni alloys can be easily prepared at different Ni/Co ratios. Ni–Mn bimetallic systems were also investigated for CO_x hydrogenation performance. The authors reported the formation of NiMnO_3 for Ni/Mn > 1 and higher activity for CO hydrogenation [11].

Cobalt and nickel have different electronic configurations. Cobalt is a d^7 metal which dissociates CO and stabilizes the vinylic intermediate. This intermediate species is stable in the sp^3 configuration, which favors the chain growth to linear hydrocarbons during FTS [2]. In contrast, nickel (d^8 metal) has a greater electronic back-donation capability. Thus, vinylic intermediates cannot be sufficiently stabilized, thereby favoring the production of light saturated hydrocarbons, especially methane. Therefore, it is of fundamental importance to investigate alloys with different Ni/Co ratios in order to determine the optimal nickel loading for (1) stabilization of the vinylic intermediate, (2) catalyst stability with time on-stream, and (3) retaining high selectivity to longer chained hydrocarbons.

Co–Ni alloys for FTS were investigated by different authors [10,12–22]. Ishihara et al. studied Co–Ni alloys supported on MnO-ZrO_2 [13] and SiO_2 [12,14]. The authors found that the electronic interactions between nickel and cobalt create new adsorption sites, which strengthen the adsorption of hydrogen and enhance the catalytic activity. Further research has suggested that nickel facilitates the reduction of cobalt, shifting it to a lower temperature, as well as increasing the dispersion of cobalt [16,18]. Moreover, Rytter et al. [18] observed that cobalt catalysts with nickel loadings up to 5 wt.% have improved stability because of the suppression of coking through nickel decoration of the cobalt surface. Recently, López-Tinoco et al. [20] characterized well-controlled nanoparticles consisting of Co–Ni alloys and compared them with a conventional heterogeneous catalyst. TPR–XANES/EXAFS showed that cobalt and nickel have an oxidation state which can be tuned from +2 to 80% metallic. However, well-controlled nanoparticles can currently be prepared in only small amounts, and as such, cannot be easily used for commercial FTS applications. The authors prepared a conventional nickel–cobalt catalyst and found similar activity to $\text{Co/Al}_2\text{O}_3$ at steady-state conditions. However, additional investigations are needed to speculate the role of nickel in these bimetallic systems.

In the present work, catalysts with different Ni/Co ratios were prepared and characterized by BET, XRD, ICP, TPR–EXAFS/XANES, and STEM. The activity and the catalytic stability have been evaluated by testing the catalysts in a CSTR reactor for more than 200 h.

2. Results

2.1. Catalyst Characterization

BET surface areas for the prepared catalysts are shown in Table 1. The surface area, pore volume, and pore diameter are similar among all the samples, suggesting that the substitution of cobalt with nickel does not affect the morphological properties. Table 1 also shows the ICP results. The cobalt loading is slightly higher ($\approx 30\%$) than the theoretical value (25%), whereas all Ni/Co ratios are consistent with the nominal values.

Table 1. BET, BJH, and ICP results for the prepared catalysts.

Sample ID	A_s (BET) [m ² /g]	V_p (BJH Des) [cm ³ /g]	D_p (BJH Des) [Å]	Co%	Ni%
25%Co	95.5	0.243	93	30.21	-
25%M—5%Ni-95%Co	92.9	0.226	91	30.49	1.43
25%M—10%Ni-90%Co	96.5	0.227	94	31.58	2.97
25%M—25%Ni-75%Co	96.0	0.236	89	24.86	7.7
25%M—50%Ni-50%Co	91.6	0.237	87	17.4	16.2

XRD patterns for Al₂O₃ and the calcined catalysts are plotted in Figure 1. All the catalysts show the characteristic reflection peaks associated with Co₃O₄ (i.e., $2\Theta = 36.8^\circ$). No diffraction peaks correlated with nickel compounds are detected for the nickel-promoted catalysts. This suggests nickel is well dispersed, as well as the formation of a Co-Ni solid oxide solution.

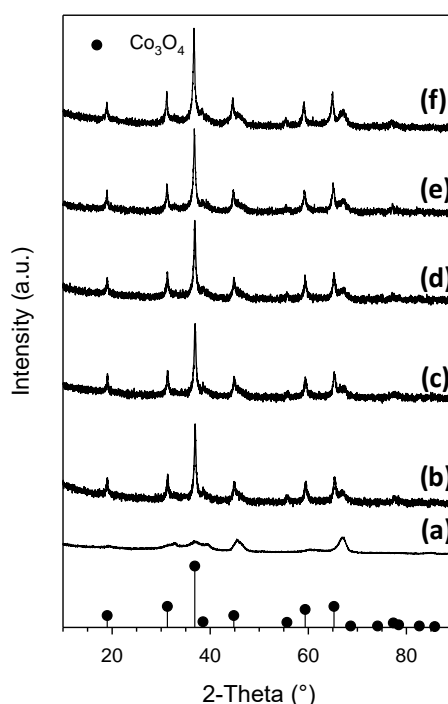


Figure 1. XRD for (a) 25%Co/Al₂O₃, (b) 25%M (M = 5%Ni-95%Co)/Al₂O₃, (c) 25%M (M = 10%Ni-90%Co)/Al₂O₃, (d) 25%M (M = 25%Ni-75%Co)/Al₂O₃, and (e) 25%M (M = 50%Ni-50%Co)/Al₂O₃.

Figure 2 shows TEM and STEM of reduced 25%M (10%Ni-90%Co)/Al₂O₃. The particle sizes are distributed between 18 and 23 nm, whereas the presence of nickel and cobalt was confirmed by EDS analysis. These two metals are uniformly distributed, consistent with the formation of a Co-Ni solid oxide solution, as suggested from XRD results. The Co/Ni weight ratio is close to 10, similar to

the theoretical value. The particle sizes for 25%Co/Al₂O₃ are between 15 and 20 nm (Figure 3). EDS analysis shows areas richer in cobalt (until 55 wt. %), and others poorer in cobalt (10 wt. %); however, the average cobalt loading is close to 28 wt. % over an extended area.

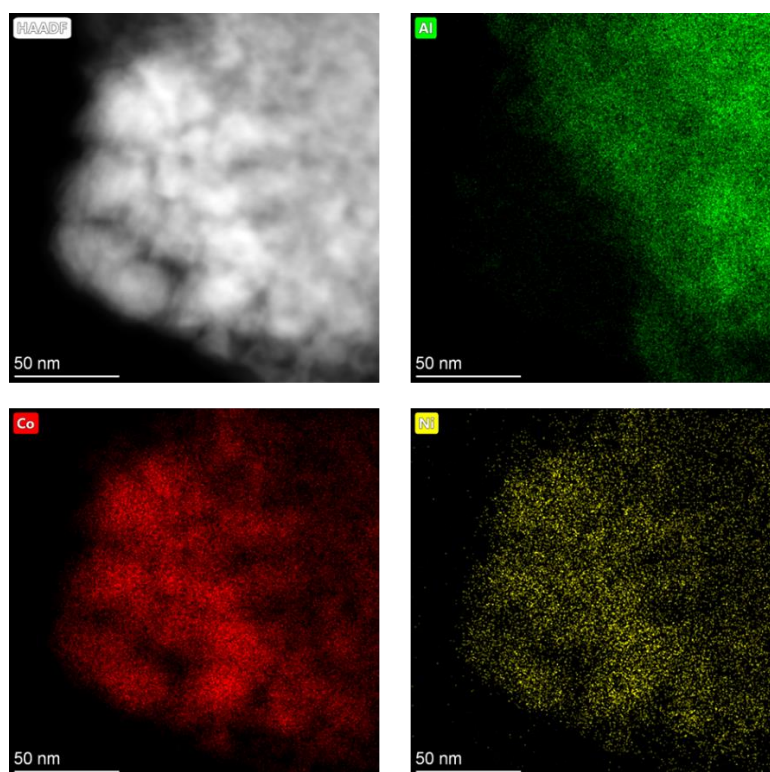


Figure 2. HAADF-STEM image of sample 25%M (10%Ni-90%Co). Elemental mapping legend: (yellow) nickel, (red) cobalt, and (green) aluminum.

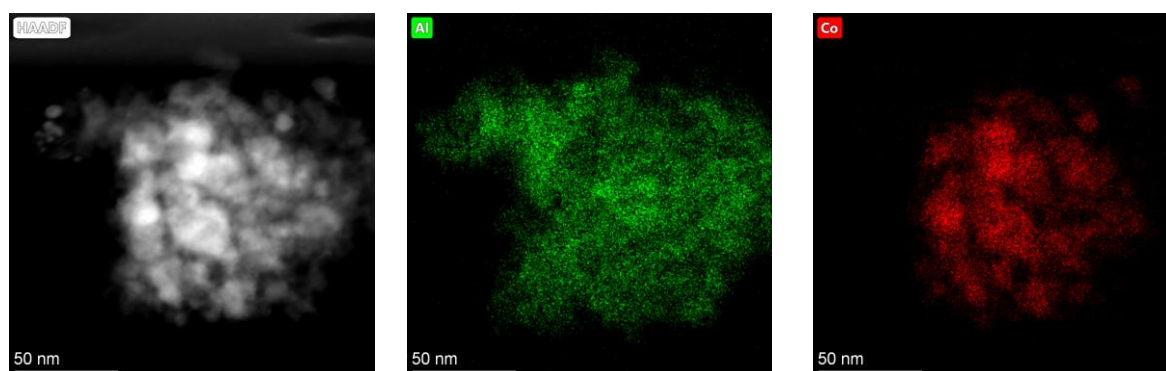


Figure 3. HAADF-STEM image of sample 25%Co. Elemental mapping legend: (green) aluminum and (red) cobalt.

Hydrogen chemisorption with pulse reoxidation results are presented in Table 2. The degree-of-reduction results are similar to those of the TPR-XANES/EXAFS data, as will be shown in the next sections. With increasing Ni/Co ratio, the mixed metal oxides exhibit more facile reduction. There also appears to be a slight increase in average metal diameter with increases in Ni/Co ratio as well. If the traditional approach, designated Method #1, of assuming complete oxidation of reduced metals to their respective oxides is used, then the increase is only slight (i.e., from 11.2 to 15.2 nm). However, if Method #2 is used, the difference is wider (i.e., from 7.0 to 13.5 nm). Method #2 assumes that, during reduction, all Co₃O₄ reduces to CoO, while only a portion of CoO reduces to Co⁰ (and a fraction of NiO reduces to Ni⁰). Thus, during the reoxidation with O₂ pulses, the Ni⁰ and Co⁰

oxidize to NiO and CoO, and all CoO (including CoO obtained from Co⁰ oxidation as well as the CoO previously resulting from merely partial reduction of Co₃O₄) oxidizes to Co₃O₄.

Table 2. H₂ chemisorption and pulse O₂ titration.

$\mu\text{mol H}_2$ desorbed/g _{cat}	Uncorr. % Disp.	Uncorr. Diam. (nm)	O ₂ Uptake (mol/g _{cat})	* % Red.	** % Red.	* Corr. % Disp.	** Corr. % Disp.	* Corr. Diam. (nm)	** Corr. Diam. (nm)
25%Co/Al ₂ O ₃ 91.3	4.3	24	1324	46.8	29.1	9.2	14.8	11.2	7.0
25%M (95%Co-5%Ni)/Al ₂ O ₃ 104.0	4.9	21.1	1317	47.3	30.4	10.4	16.1	10.0	6.4
25%M (90%Co-10%Ni)/Al ₂ O ₃ 92.5	4.4	24	1495	54.6	40.5	8.0	10.8	12.9	9.6
25%M (75%Co-25%Ni)/Al ₂ O ₃ 94.6	4.5	23.2	1563	59.9	48.7	7.5	9.2	13.9	11.3
25%M (50%Co-50%Ni)/Al ₂ O ₃ 94.7	4.5	23.1	1594	65.7	58.5	6.8	7.6	15.2	13.5

* Method #1 assuming Ni⁰ oxidizes to NiO and Co⁰ oxidizes to Co₃O₄. ** Method #2 assuming all Co₃O₄ reduced to CoO and some NiO and CoO reduced to Ni⁰ and Co⁰. During oxidation, then, the Ni⁰ and Co⁰ oxidize to NiO and CoO, and all CoO oxidizes to Co₃O₄.

2.2. Cobalt Reducibility

2.2.1. H₂ TPR-XANES

Figures 4 and 5 display H₂ TPR-XANES spectra for the prepared samples at the Co K-edge as a function of increasing Ni/Co ratio using two different perspectives. The perspective of Figure 4 is versus temperature, whereas the perspective of Figure 5 is that of photon energy. XANES snapshots at the point of 100% Co₃O₄, 100% CoO, as well as the final spectrum at the point of maximum reduction to Co⁰, are shown in Figure 6. Cobalt oxides reduce to metallic compounds in two steps: (I) Co₃O₄ + H₂ = 3CoO + H₂O and (II) 3CoO + 3H₂ = 3Co⁰ + 3H₂O. Figure 6 shows that with increasing Ni/Co ratio, the reduction of cobalt oxides systematically moves to lower temperature.

Linear combination XANES fittings at the Co K-edge are provided in Figure 7. For all of the catalysts, the initial spectrum at 25 °C resembles that of Co₃O₄. The point of 50%Co₃O₄/50%CoO was reached at 339 °C (Ni/Co = 0/100), 308 °C (Ni/Co = 5/95), 294 °C (Ni/Co = 10/90), 273 °C (Ni/Co = 25/75), and 249 °C (Ni/Co = 50/50). Thus, up to a Δ 90 °C decrease in reduction temperature was achieved. The point of 100%CoO was obtained at 400 °C (Ni/Co = 0/100), 330 °C (Ni/Co = 5/95), 330 °C (Ni/Co = 10/90), 305 °C (Ni/Co = 25/75), and 278 °C (Ni/Co = 50/50). Thus, up to a Δ 122 °C decrease in reduction temperature was obtained in converting Co₃O₄ to CoO by increasing the Ni/Co ratio.

The point of 50%CoO/50%Co⁰ was attained at 553 °C (Ni/Co = 0/100), 473 °C (Ni/Co = 5/95), 473 °C (Ni/Co = 10/90), 437 °C (Ni/Co = 25/75), and 386 °C (Ni/Co = 50/50). Thus, up to a Δ 167 °C decrease in reduction temperature was achieved by doping Co with Ni. It is evident that, unlike the Group 10 metal Pt, where substantial shifts in the reduction of Co oxides were observed with minute amounts of Pt, significantly higher quantities of Ni are required to achieve the same level of reduction. For example, just 0.5%Pt was able to facilitate a decrease of 194 °C for the Co₃O₄ to CoO transition, and a decrease of 120 °C from CoO to Co⁰ [23], this amount of Pt is 1/80th the atomic amount of Ni for the 25% metal catalyst having Ni/Co = 50/50. Considering the case of CoO reduction during reduction of undoped 25%Co/Al₂O₃, where TPR-XANES reveal strong interactions with the support, the higher loading required for Ni to facilitate reduction (i.e., compared to Pt) is likely due in part to the strong interactions between Ni oxides and alumina support.

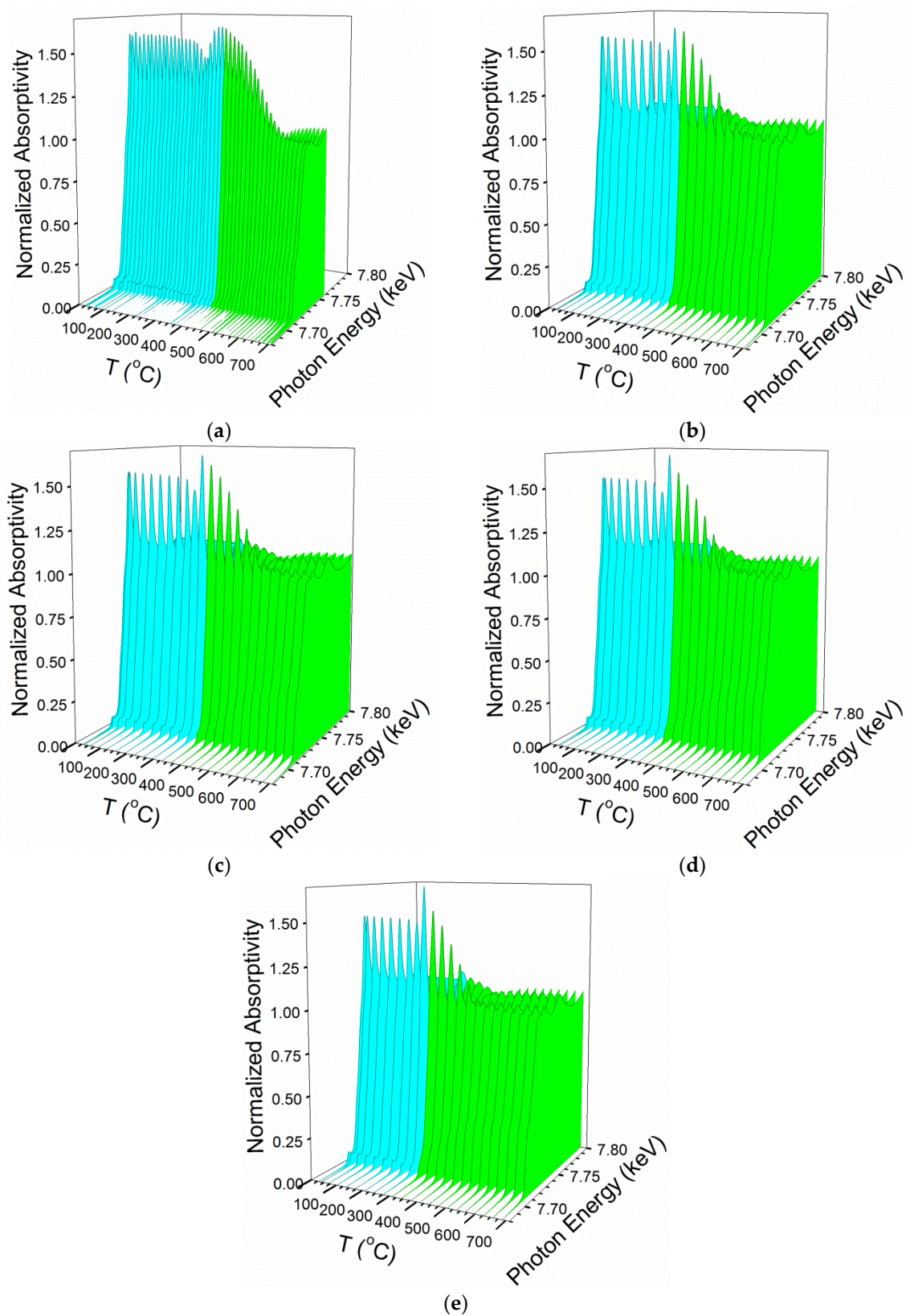


Figure 4. H₂-TPR-XANES spectra at the Co K-edge of (a) 25%Co/Al₂O₃, (b) 25%M (M = 5%Ni-95%Co)/Al₂O₃, (c) 25%M (M = 10%Ni-90%Co)/Al₂O₃, (d) 25%M (M = 25%Ni-75%Co)/Al₂O₃, and (e) 25%M (M = 50%Ni-50%Co)/Al₂O₃.

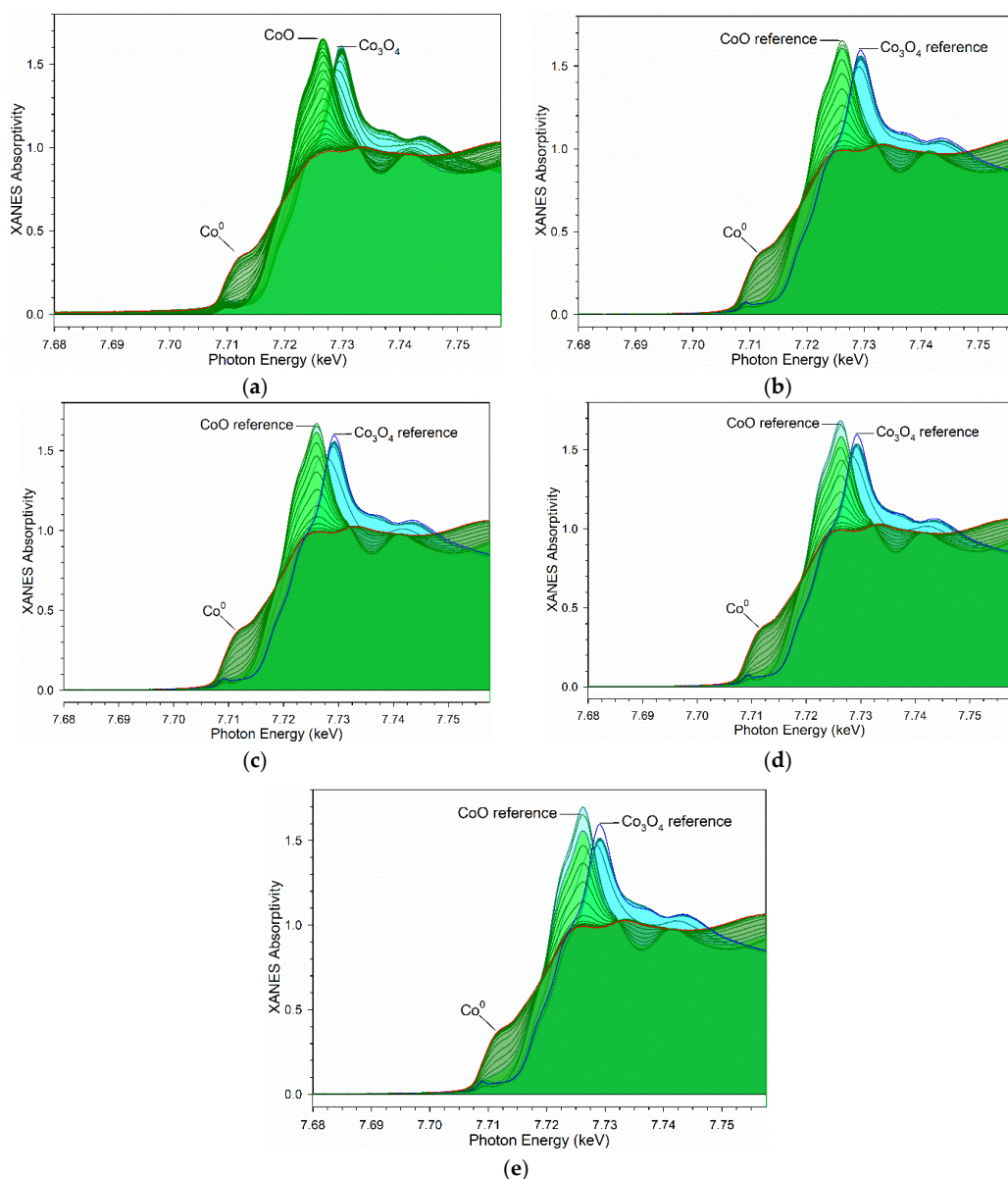


Figure 5. H₂-TPR-XANES spectra (XY view) at the Co K-edge of (a) 25%Co/Al₂O₃, (b) 25%M (M = 5%Ni-95%Co)/Al₂O₃, (c) 25%M (M = 10%Ni-90%Co)/Al₂O₃, (d) 25%M (M = 25%Ni-75%Co)/Al₂O₃, and (e) 25%M (M = 50%Ni-50%Co)/Al₂O₃.

2.2.2. H₂ TPR-EXAFS

TPR-EXAFS spectra at the Co K-edge are shown in Figures 8 and 9, including a plot that highlights the temperature (Figure 8), and a plot that emphasizes differences as a function of distance from the absorber (Figure 9). The initial cyan spectrum of each TPR-EXAFS profile represents Co₃O₄. It can be differentiated from CoO (i.e., the first green spectrum) by the fact that the Co–O peak is significantly more intense, while the Co–Co coordination peak is broadened due to the presence of additional oxygen atoms (Figure 9). Following the transition to CoO, the CoO slowly converts to Co⁰, resulting in a final well-resolved peak for Co–Co metal coordination. In a manner similar to Pt and Ru promoters, Ni facilitates both steps of reduction; however, as mentioned previously, on an atomically equivalent basis, Ni is far less effective than either Pt or Ru [23]. It differs from Re, which only catalyzes the second step, CoO reduction to Co⁰. Unlike Pt and Ru oxides, which reduce at low temperatures, Re oxide was observed to reduce at a similar range as Co₃O₄ reduction to CoO (i.e., 300–350 °C), and it was supposed that a reduced form was necessary in order to facilitate CoO reduction through a H₂ dissociation and

spillover mechanism [23]. Thus, if a hydrogen dissociation and spillover mechanism operated for the case of Ni, one would expect that NiO should reduce to Ni⁰ prior to the reduction of Co oxides. Based on the Ni X-ray absorption spectroscopy results, this does not seem to be the case.

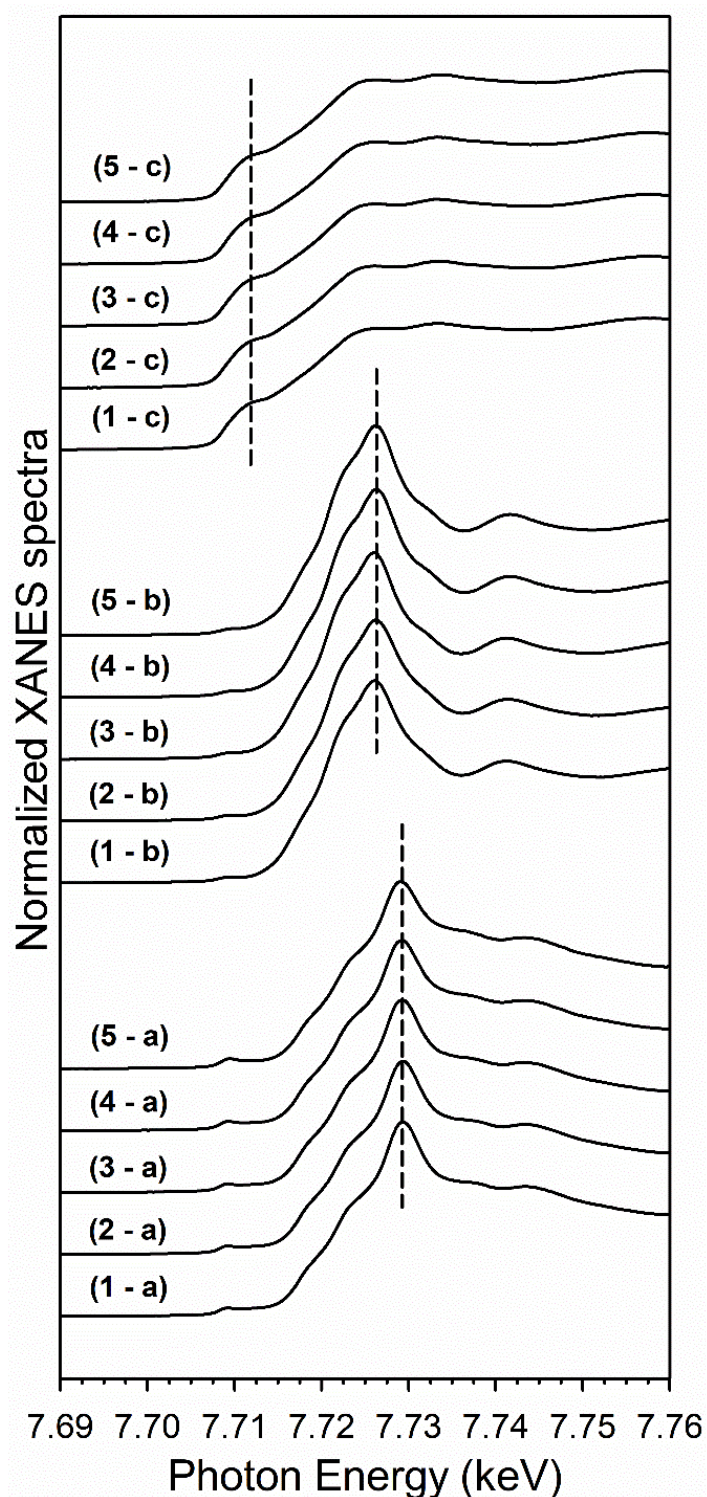


Figure 6. Co K-edge XANES spectra: (a) the initial point consisting of primarily Co₃O₄; (b) the point of maximum CoO content; and (c) the final spectrum consisting of primarily Co⁰ for (1) 25%Co/Al₂O₃, (2) 25%M (M = 5%Ni-95%Co)/Al₂O₃, (3) 25%M (M = 10%Ni-90%Co)/Al₂O₃, (4) 25%M (M = 25%Ni-75%Co)/Al₂O₃, and (5) 25%M (M = 50%Ni-50%Co)/Al₂O₃.

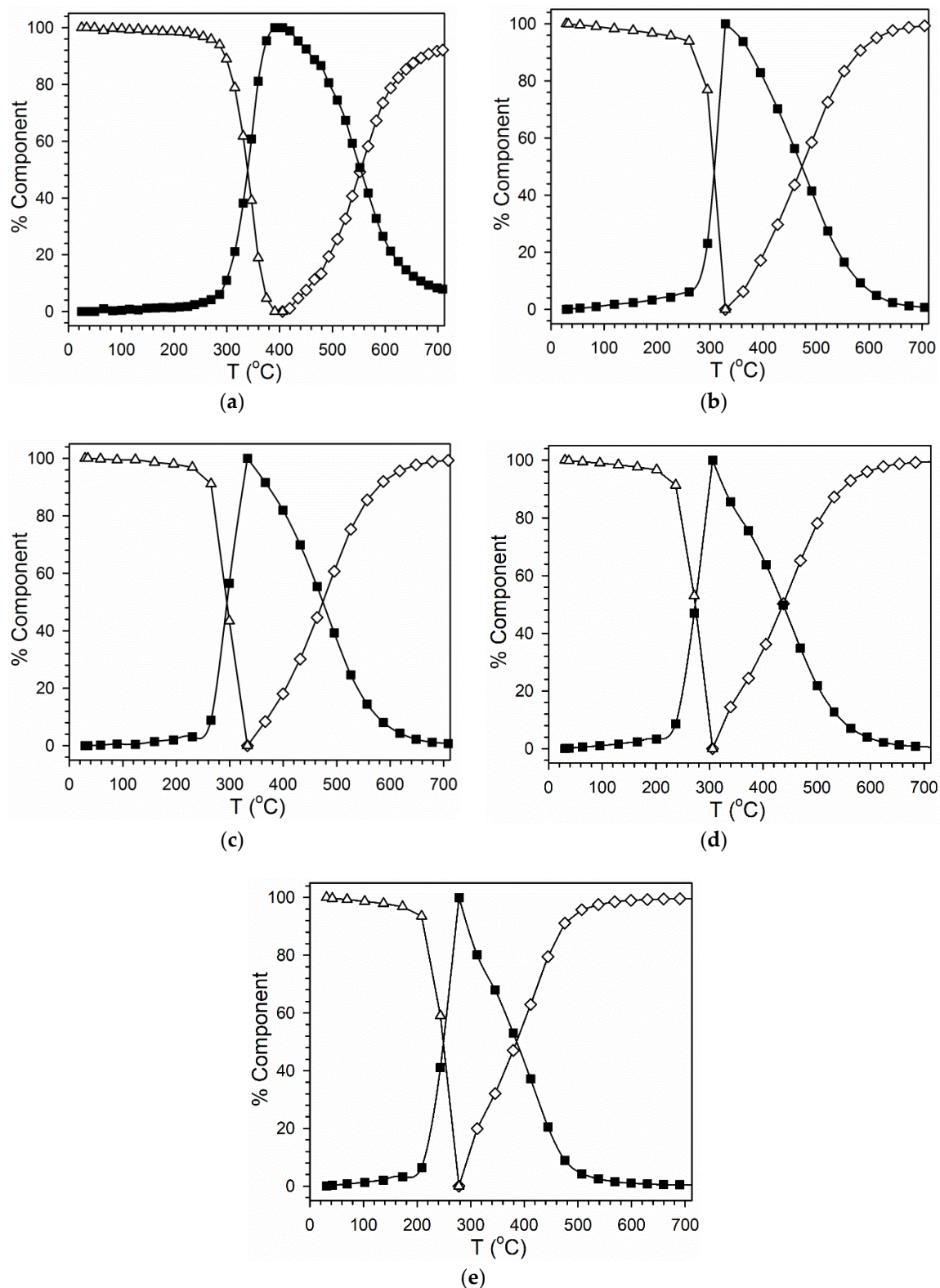


Figure 7. LC fittings of H₂-TPR-XANES spectra at the Co K-edge of (a) 25%Co/Al₂O₃, (b) 25%M (M = 5%Ni-95%Co)/Al₂O₃, (c) 25%M (M = 10%Ni-90%Co)/Al₂O₃, (d) 25%M (M = 25%Ni-75%Co)/Al₂O₃, and (e) 25%M (M = 50%Ni-50%Co)/Al₂O₃.

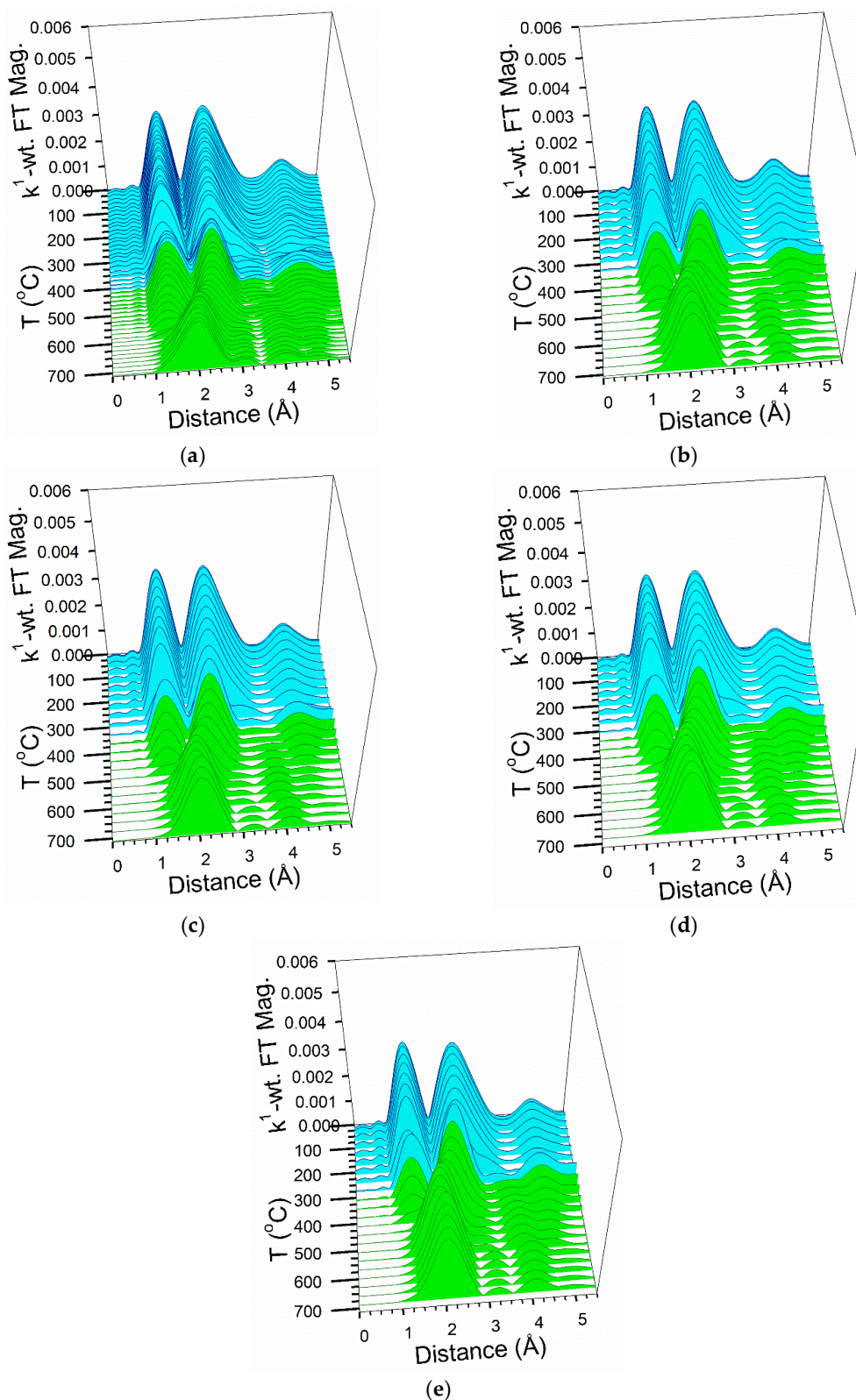


Figure 8. H₂-TPR-EXAFS spectra at the Co K-edge of (a) 25%Co/Al₂O₃, (b) 25%M (M = 5%Ni-95%Co)/Al₂O₃, (c) 25%M (M = 10%Ni-90%Co)/Al₂O₃, (d) 25%M (M = 25%Ni-75%Co)/Al₂O₃, and (e) 25%M (M = 50%Ni-50%Co)/Al₂O₃. (Cyan) is reduction of Co₃O₄ to CoO, and (Green) CoO to Co⁰.

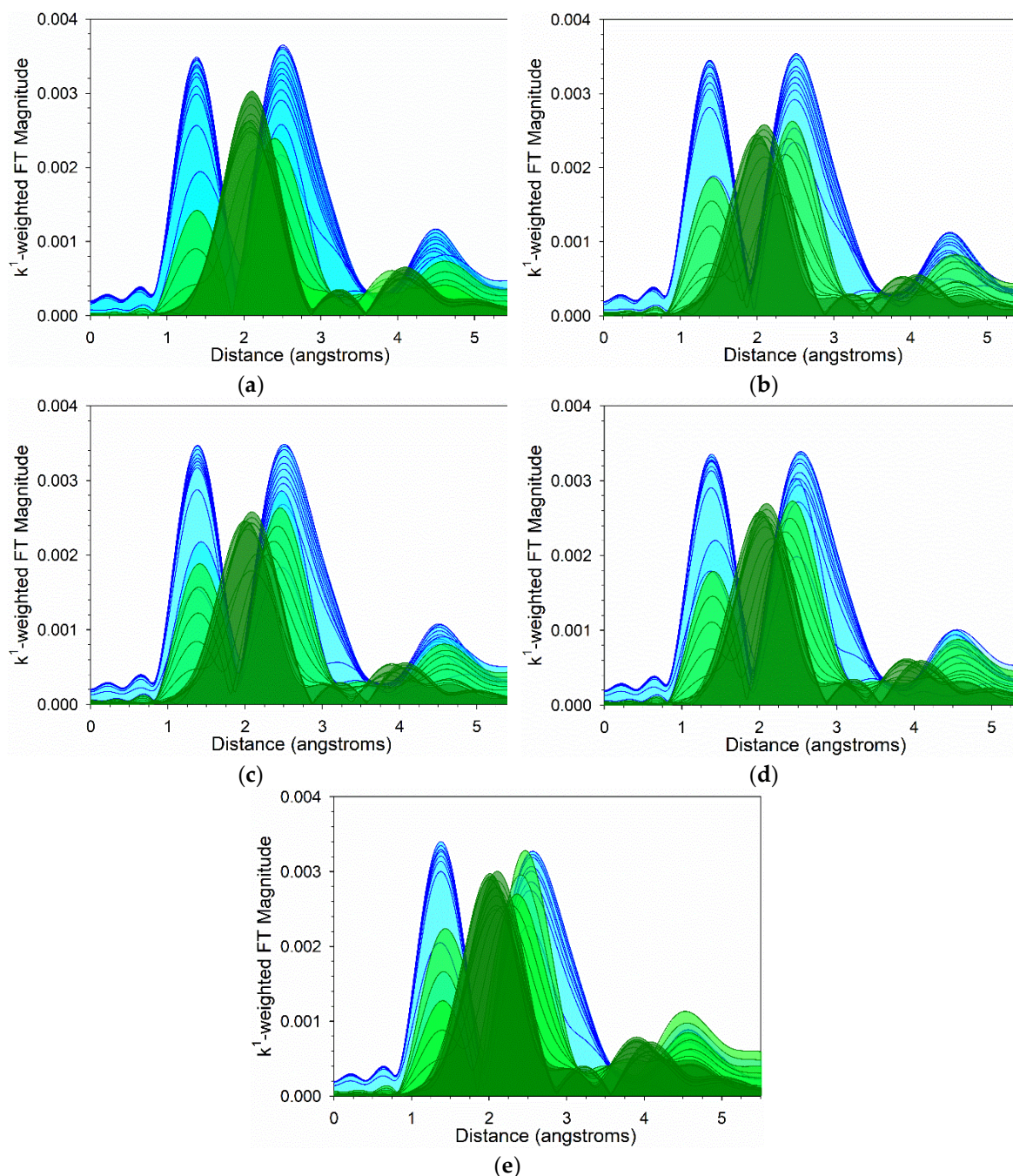


Figure 9. H_2 -TPR-EXAFS spectra (XY view) at the Co K-edge of (a) 25%Co/ Al_2O_3 , (b) 25%M (M = 5%Ni-95%Co)/ Al_2O_3 , (c) 25%M (M = 10%Ni-90%Co)/ Al_2O_3 , (d) 25%M (M = 25%Ni-75%Co)/ Al_2O_3 , and (e) 25%M (M = 50%Ni-50%Co)/ Al_2O_3 . (Cyan) is reduction of Co_3O_4 to CoO , and (Green) CoO to Co^0 .

EXAFS snapshots of the different chemical species (e.g., Co_3O_4 , CoO , and Co^0), observed during the TPR trajectory, are provided in Figure 10. Structural similarities are evidenced by the common peak positions for Co-O and Co-Co coordination. The only differences among the samples are in the temperatures at which the CoO and Co^0 evolve, as previously discussed in the TPR-XANES section.

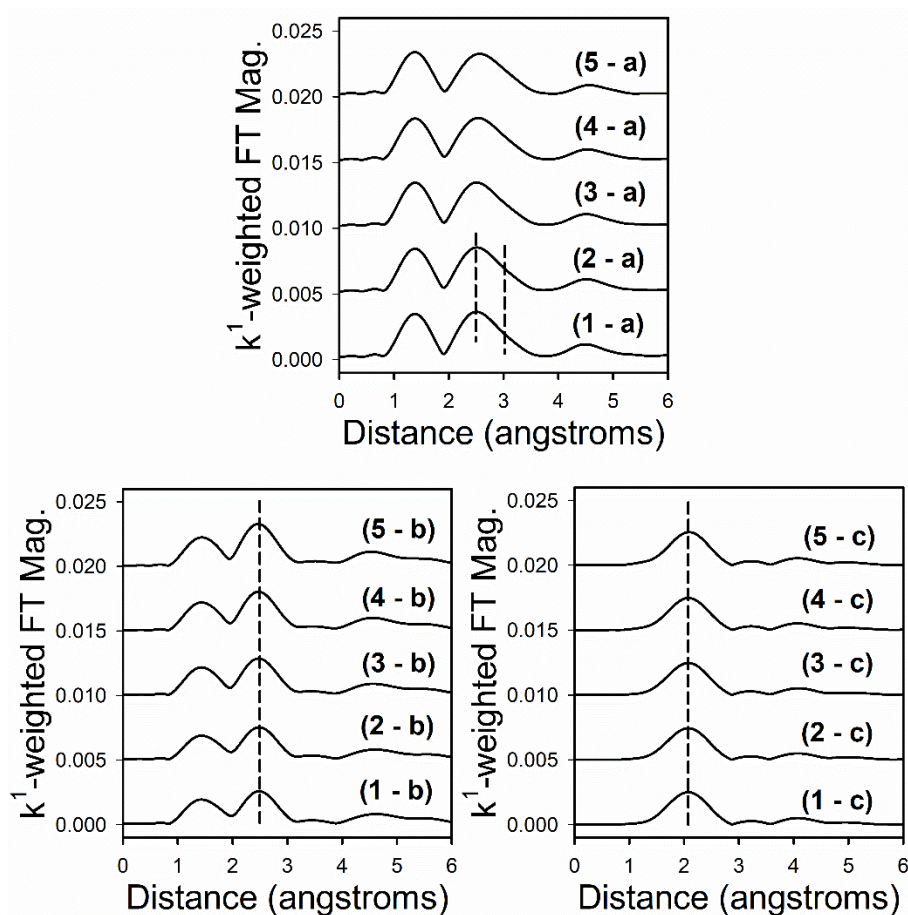


Figure 10. Co K-edge EXAFS spectra of (a) the initial point consisting of primarily Co_3O_4 , (b) the point of maximum CoO content, and (c) the final spectrum consisting of primarily Co^0 for (1) 25%Co/ Al_2O_3 , (2) 25%M (M = 5%Ni-95%Co)/ Al_2O_3 , (3) 25%M (M = 10%Ni-90%Co)/ Al_2O_3 , (4) 25%M (M = 25%Ni-75%Co)/ Al_2O_3 , (5) 25%M (M = 50%Ni-50%Co)/ Al_2O_3 .

2.3. Nickel Reducibility

2.3.1. H_2 TPR-XANES

TPR-XANES spectra in Figures 11 and 12 at the Ni K-edge reveal that, initially, Ni oxide is associated with Co_3O_4 (see spectra in cyan color), and this Ni oxide subsequently undergoes a change in electronic structure to a form of Ni oxide associated with CoO (initial green spectrum). This change is best observed by examining the head-on spectra of Figure 13, as well as the XANES snapshots shown in Figure 14. Let us refer to this transition as step one. Step two is further reduction of Ni^{2+} to Ni^0 (dark green spectra in Figure 12).

Figure 14 provides quantitative information regarding the Ni species present along the TPR trajectory. In step one, the point of 50% Ni^{2+} - Co_3O_4 / 50% Ni^{2+} -CoO was reached at 333 °C (Ni/Co = 5/95), 286 °C (Ni/Co = 10/90), 261 °C (Ni/Co = 25/75), and 234 °C (Ni/Co = 50/50). Thus, up to a Δ 99 °C decrease in reduction temperature was achieved (compared to a Δ of 60 °C for the cobalt system over the same range of loading), and the temperatures match well with those of the Co_3O_4 to CoO transitions described earlier at the 50% point of conversion, especially at higher Ni/Co ratios. The point of 100% Ni^{2+} -CoO was obtained at 362 °C (Ni/Co = 5/95), 332 °C (Ni/Co = 10/90), 305 °C (Ni/Co = 25/75), and 278 °C (Ni/Co = 50/50). Thus, up to a Δ 84 °C decrease in reduction temperature was obtained in converting 100% Ni^{2+} - Co_3O_4 to 100% Ni^{2+} -CoO (compared to a Δ of 52 °C for the cobalt system over the same range of loading). Once again, the temperatures match quite well with those of the Co_3O_4 to

CoO transitions described earlier for Co K-edge data, and match nearly perfectly at Ni/Co loadings of 10%, 25%, and 50%.

Continuing, the point of 50%Ni²⁺-CoO/50%Ni⁰ was achieved at 503 °C (Ni/Co = 5/95), 482 °C (Ni/Co = 10/90), 458 °C (Ni/Co = 25/75), and 412 °C (Ni/Co = 50/50). Thus, up to a Δ 91 °C decrease in reduction temperature was achieved by doping Co with Ni (compared to a Δ of 87 °C for the cobalt system over the same range of loading).

The similarities in temperature ranges between Co₃O₄ to CoO and the Ni²⁺-Co₃O₄ to Ni²⁺-CoO transitions, as well those between CoO to Co⁰ and Ni²⁺-CoO to Ni⁰-Co⁰ transitions, suggest that the effect may not be simply a H₂ dissociation and spillover mechanism, but rather a chemical effect due to intimate contact between Ni and Co in both oxide (e.g., solid solution) and metallic (e.g., alloy) phases, throughout the TPR trajectory.

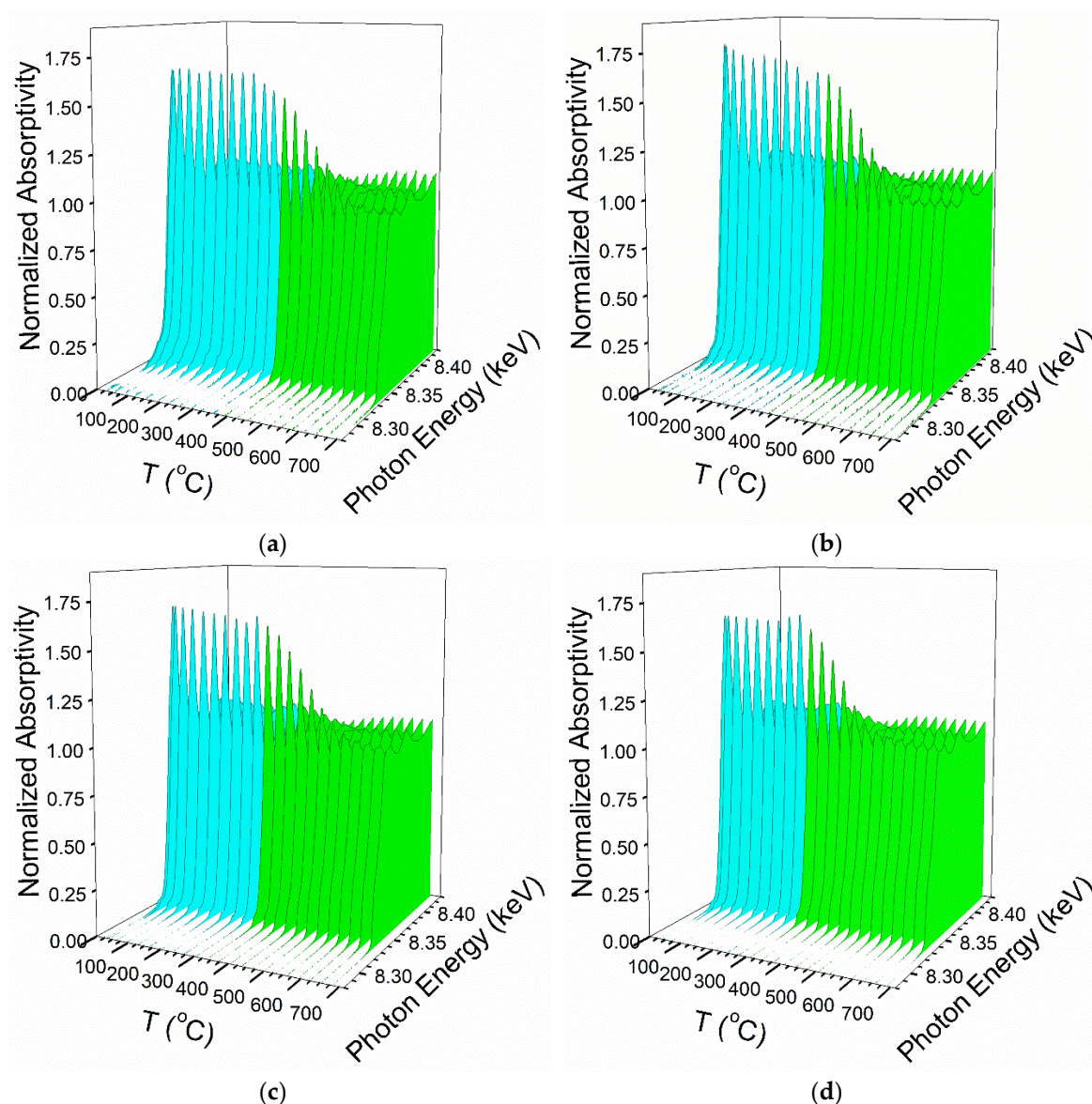


Figure 11. H₂-TPR-XANES spectra at the Ni K-edges of (a) 25%M (M = 5%Ni-95%Co)/Al₂O₃, (b) 25%M (M = 10%Ni-90%Co)/Al₂O₃, (c) 25%M (M = 25%Ni-75%Co)/Al₂O₃, and (d) 25%M (M = 50%Ni-50%Co)/Al₂O₃. (Cyan) is Ni²⁺ (e.g., NiO) associated with cobalt oxides during reduction of Co₃O₄ to CoO. (Green) is reduction of Ni²⁺ to Ni⁰ when NiO reduction is associated with CoO reduction to Co⁰.

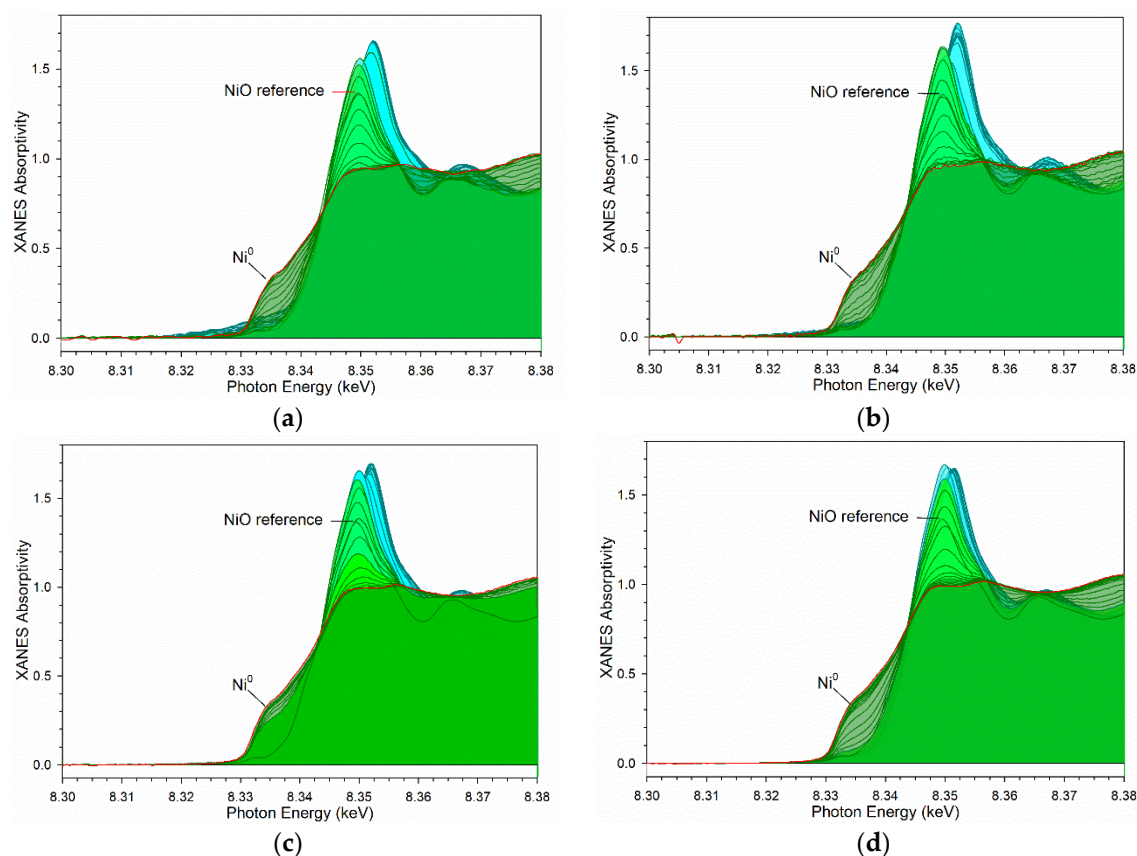


Figure 12. H₂-TPR-XANES spectra at the Ni K-edges of (a) 25%M (M = 5%Ni-95%Co)/Al₂O₃, (b) 25%M (M = 10%Ni-90%Co)/Al₂O₃, (c) 25%M (M = 25%Ni-75%Co)/Al₂O₃, and (d) 25%M (M = 50%Ni-50%Co)/Al₂O₃. (Cyan) is Ni²⁺ (e.g., NiO) associated with cobalt oxides during reduction of Co₃O₄ to Co⁰. (Green) is reduction of Ni²⁺ to Ni⁰ when NiO reduction is associated with CoO reduction to Co⁰.

2.3.2. H₂ TPR-EXAFS

Comparing the TPR-EXAFS spectra of Figure 15 with Figure 8, Figure 16 with Figure 9, and Figure 17 with Figure 10, it is remarkable how closely the behavior of Ni resembles that of Co. The initial cyan spectra of Figures 15 and 16 reveal that the first Ni–O peak is more intense than that of the green Ni–O peak, suggesting greater coordination to oxygen, while the second peak for Ni–Ni coordination in the initial cyan spectra is more broadened compared to the initial green spectra, consistent with greater oxygen content forcing Ni atoms apart. Figure 17 highlights the differences between the local atomic structures of different species along the TPR profile (e.g., Ni²⁺ associated with Co₃O₄; Ni²⁺ associated with CoO; and Ni⁰ associated with Co⁰).

Figures 18 and 19, as well as Table 3, show EXAFS fittings for the Co K-edge and Ni K-edge data following TPR-EXAFS and cooling to ambient temperature. A simple model was developed previously [20] and applied here, wherein metal coordination to Ni (whether the core atom was Co or Ni) was given as a fraction, *X*, of metal-cobalt coordination. Using this approach, excellent fittings with low *r*-factors were obtained. Co–Ni alloy formation is consistent with EXAFS fitting, but it cannot be considered proven, since Co and Ni are too closely related in size.

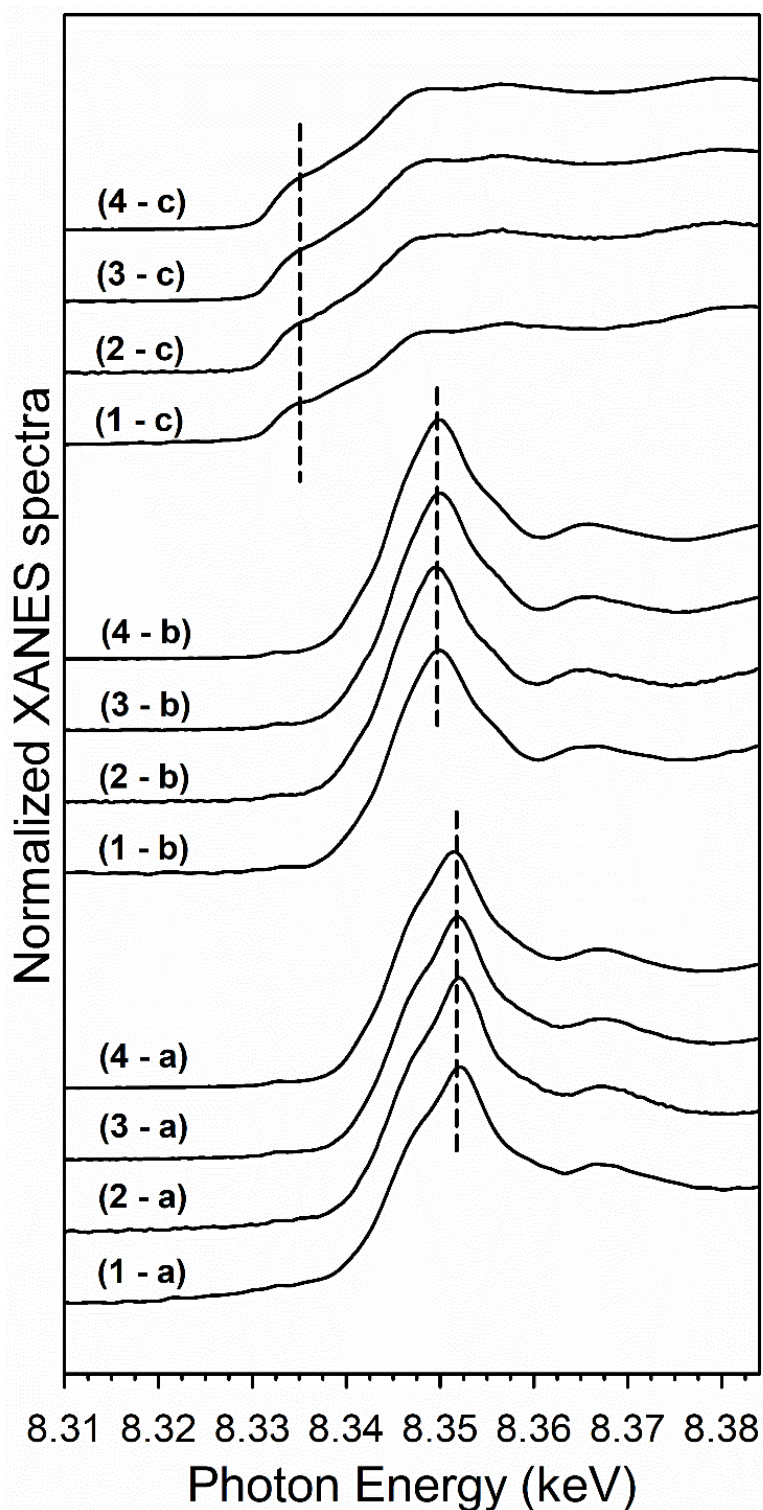


Figure 13. Ni K-edge XANES spectra of (a) the initial point consisting of primarily NiO associated with Co_3O_4 , (b) the point consisting of primarily NiO associated with CoO, and (c) the final spectrum consisting of primarily Ni^0 for (2) 25%M (M = 5%Ni-95%Co)/ Al_2O_3 , (3) 25%M (M = 10%Ni-90%Co)/ Al_2O_3 , (4) 25%M (M = 25%Ni-75%Co)/ Al_2O_3 .

Table 3. Results of EXAFS fitting* for data acquired near the Co and Ni K edges for catalysts following TPR-EXAFS after cooling. The fitting ranges were $\Delta k = 3\text{--}10 \text{ \AA}^{-1}$ and $\Delta R = 1.2\text{--}2.8 \text{ \AA}$. * S_0^2 set to 0.90. Mixing parameter fixed to nominal value.

Sample Description	N Co-Co Metal	R Co-Co (\AA) Metal	N Co-Ni Metal	R Co-Ni (\AA) Metal	N Ni-Ni Metal	R Ni-Ni (\AA) Metal	N Ni-Co Metal	R Ni-Co (\AA) Metal	e_0 (eV)	σ^2 (\AA^2)	r-factor
100Co	9.9	2.489 (0.003)	-	-	-	-	-	-	6.37 (0.45)	0.00731 (0.00043)	0.0010
5Ni:95Co	9.9 (0.78)	2.489 (0.0053)	0.50 (0.04)	2.481 (0.0053)	0.32 (0.03)	2.472 (0.0053)	6.3 (0.59)	2.481 (0.0053)	6.32 (0.813)	0.00787 (0.00076)	0.014
10Ni:90Co	9.4 (0.48)	2.492 (0.0034)	0.94 (0.05)	2.483 (0.0034)	0.75 (0.04)	2.475 (0.0034)	7.5 (0.41)	2.483 (0.0034)	6.56 (0.527)	0.00777 (0.00048)	0.0035
25Ni:75Co	8.0 (0.31)	2.491 (0.0026)	2.0 (0.08)	2.482 (0.0026)	1.9 (0.08)	2.474 (0.0026)	7.4 (0.32)	2.482 (0.0026)	6.71 (0.401)	0.00719 (0.00036)	0.0023
50Ni:50Co	6.5 (0.36)	2.491 (0.0035)	3.3 (0.18)	2.483 (0.0035)	3.2 (0.18)	2.475 (0.0035)	6.4 (0.36)	2.483 (0.0035)	-4.39 (0.613)	0.00659 (0.00049)	0.0034

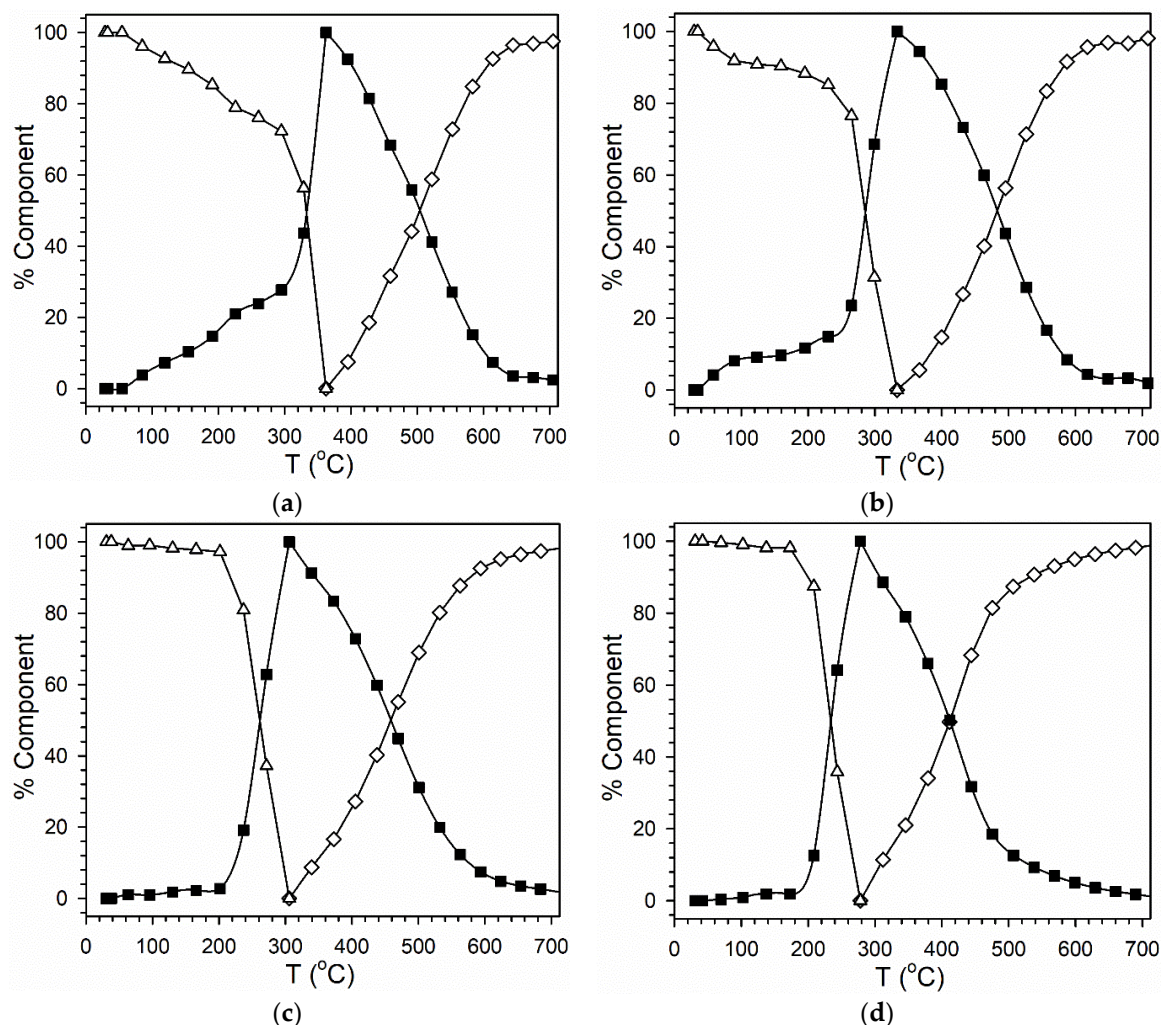


Figure 14. LC fittings of H₂-TPR-XANES spectra at the Ni K-edge of (a) 25%M (M = 5%Ni-95%Co)/Al₂O₃, (b) 25%M (M = 10%Ni-90%Co)/Al₂O₃, (c) 25%M (M = 25%Ni-75%Co)/Al₂O₃, and (d) 25%M (M = 50%Ni-50%Co)/Al₂O₃. Legend: Δ Ni²⁺ associated with Co₃O₄, \blacksquare Ni²⁺ associated with CoO, and \diamond Ni⁰ associated with Co⁰.

2.4. Catalytic Activity

CO conversion in the first 200 h is shown in Figure 20. The CO conversion for the unpromoted catalyst has an initial value of 42.5%, and then it slightly decreases in the first few hours until a steady-state value of 39.5% was reached. This trend is typical for cobalt-based catalysts. In contrast, CO conversion progressively increases for all nickel-promoted catalysts. 5%Ni-95%Co and 10%Ni-90%Co exhibit similar CO conversion trends, as the former's initial value is close to 20%, and it continuously increases, reaching 34%, whereas 25%Ni-75%Co has a higher initial CO conversion (29%), and it reaches a steady-state value of 36%.

The evolutions of selectivities (CH₄, CO₂, C₂-C₄, and C₅₊) with T.o.S. (time on-stream) are shown in Figure 21. CH₄ selectivity and C₅₊ selectivities are stable at 7.6% and 80.7%, respectively, for the unpromoted catalyst. The addition of nickel increases initial CH₄ selectivity, whereas it decreases initial C₅₊ selectivity. Fortunately, CH₄ selectivity for the nickel-promoted catalyst slowly decreased with T.o.S. For example, the initial CH₄ selectivity for 25%M—25%Ni-75%Co is 13.4%, but it reaches 9.5% after 200 h. Thus, the difference compared to Co/Al₂O₃ decreases from 5.8% (absolute) to just 1.9%.

The olefin/paraffin ratio for unpromoted and nickel-promoted catalysts decreases with increasing carbon number, starting with ethylene species and moving upward (Figure 22). This trend is typically observed for cobalt based catalysts. However, even if the trend with the carbon number is similar

among the different catalysts, the olefin content decreases by increasing the nickel content. Indeed, the olefin/paraffin ratio for C_3 species is 2.5 for 25%Co, while it is only 1 for the 25%M—75%Co-25%Ni catalyst. At higher carbon numbers, the differences among the different Ni/Co catalysts are not so pronounced because of the tendency of olefins to readsorb on active sites [24]. The high hydrogenation capability of nickel promoted samples is also observed by a slight decrease in chain growth probability. Indeed $\alpha_{C_5-C_{16}}$ slightly decreases from 0.85 for 25%Co to 0.83 for 25%M—25%Ni-75%Co.

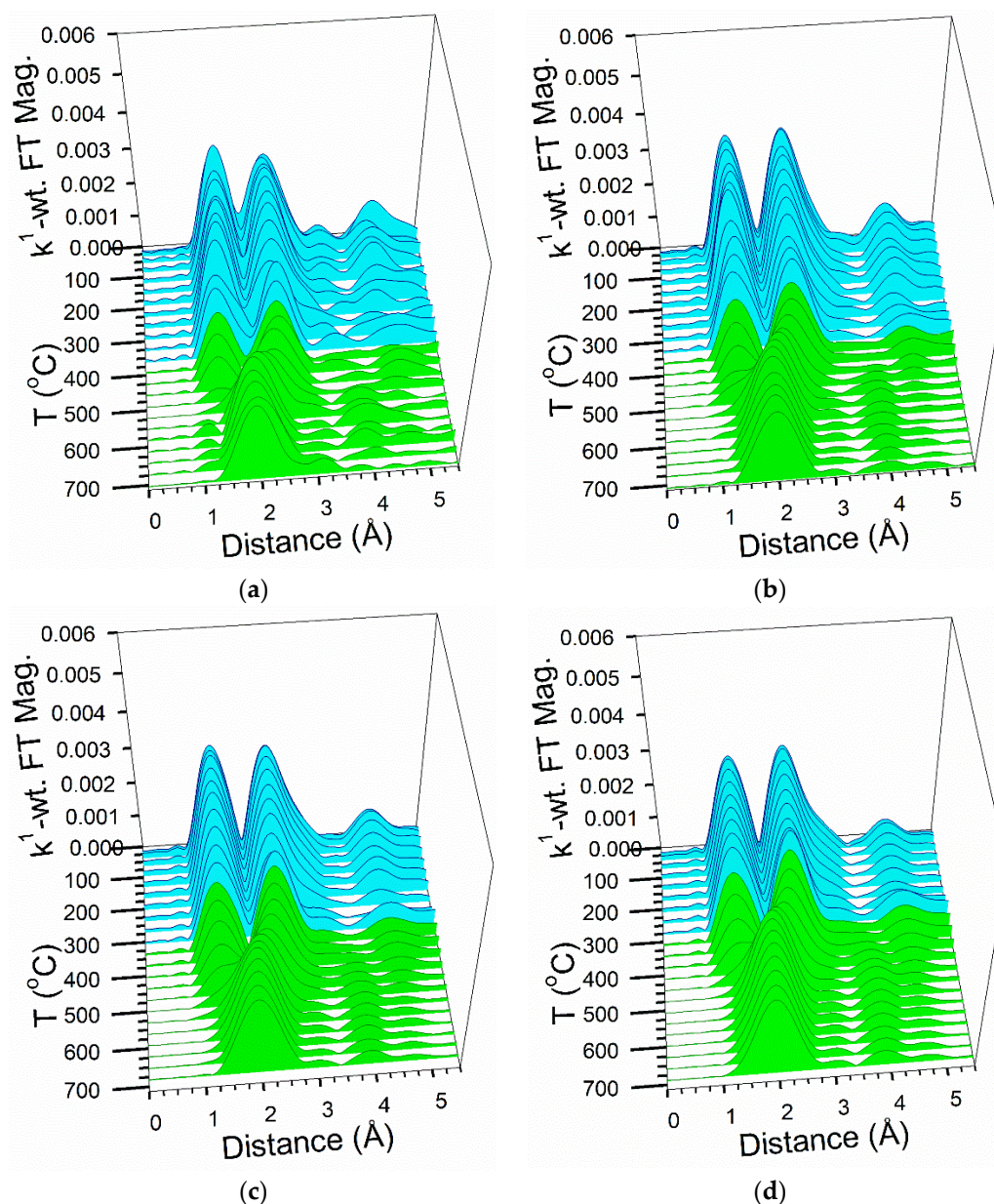


Figure 15. H_2 -TPR-EXAFS spectra at the Ni K-edges of (a) 25%M (M = 5%Ni-95%Co)/ Al_2O_3 , (b) 25%M (M = 10%Ni-90%Co)/ Al_2O_3 , (c) 25%M (M = 25%Ni-75%Co)/ Al_2O_3 , and (d) 25%M (M = 50%Ni-50%Co)/ Al_2O_3 . (Cyan) is Ni^{2+} (e.g., NiO) associated with cobalt oxides during reduction of Co_3O_4 to CoO. (Green) is reduction of Ni^{2+} to Ni^0 when NiO reduction is associated with CoO reduction to Co^0 .

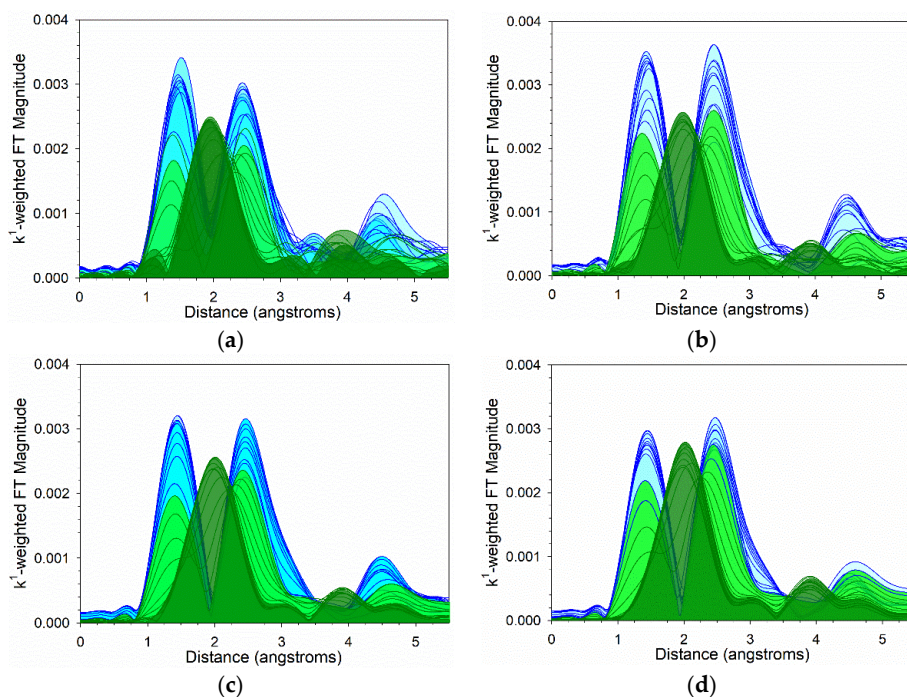


Figure 16. H₂-TPR-EXAFS spectra at the Ni K-edges of (a) 25%M (M = 5%Ni-95%Co)/Al₂O₃, (b) 25%M (M = 10%Ni-90%Co)/Al₂O₃, (c) 25%M (M = 25%Ni-75%Co)/Al₂O₃, and (d) 25%M (M = 50%Ni-50%Co)/Al₂O₃. (Cyan) is Ni²⁺ (e.g., NiO) associated with cobalt oxides during reduction of Co₃O₄ to CoO. (Green) is reduction of Ni²⁺ to Ni⁰ when NiO reduction is associated with CoO reduction to Co⁰.

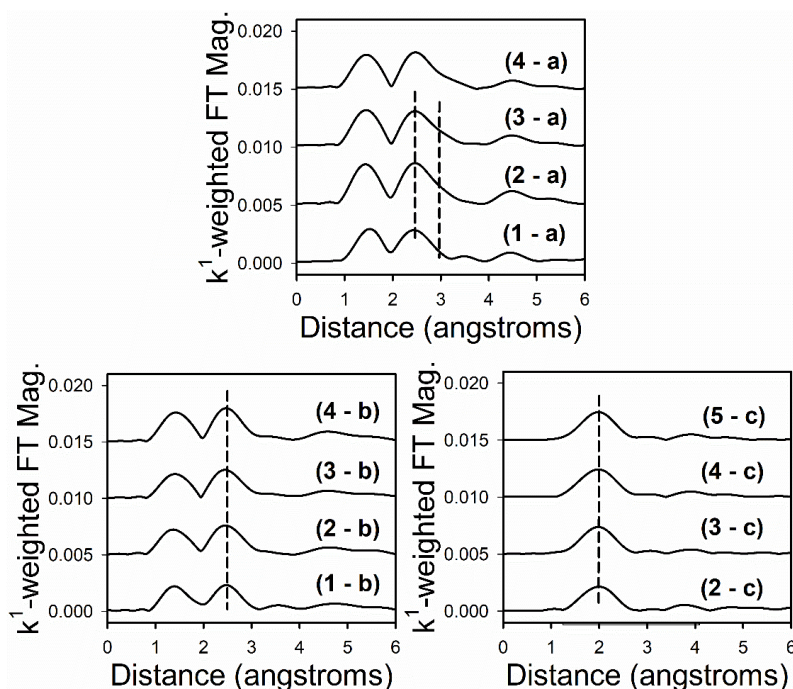


Figure 17. Ni K-edge EXAFS spectra: (a) the initial point consisting of primarily NiO associated with Co₃O₄; (b) the point consisting of primarily NiO associated with CoO; and (c) the final spectrum consisting of primarily Ni⁰ for (2) 25%M (M = 5%Ni-95%Co)/Al₂O₃, (3) 25%M (M = 10%Ni-90%Co)/Al₂O₃, (4) 25%M (M = 25%Ni-75%Co)/Al₂O₃, and (5) 25%M (M = 50%Ni-50%Co)/Al₂O₃.

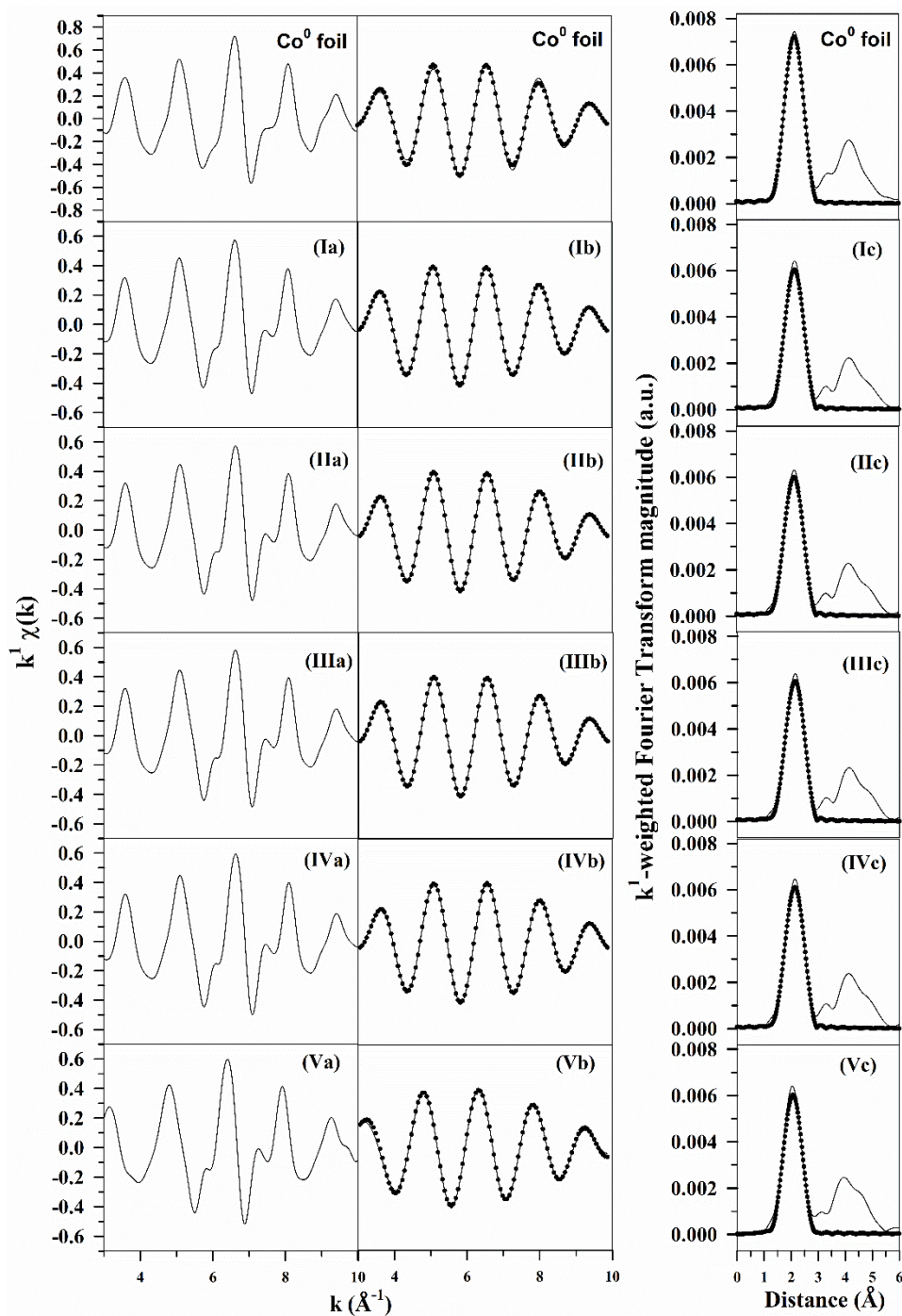


Figure 18. EXAFS fittings for Co K-edge data, including (a) raw k^1 -weighted $\chi(k)$ data; (b) (solid line) filtered k^1 -weighted $\chi(k)$ data and (filled circles) results of the fittings; (c) (solid line) raw k^1 -weighted Fourier transform magnitude and (solid line) filtered k^1 -weighted Fourier transform magnitude; and (filled circles) results of the fittings for Co^0 foil, (I) 25%Co/ Al_2O_3 , (II) 25%M (M = 5%Ni-95%Co)/ Al_2O_3 , (III) 25%M (M = 10%Ni-90%Co)/ Al_2O_3 , (IV) 25%M (M = 25%Ni-75%Co)/ Al_2O_3 , and (V) 25%M (M = 50%Ni-50%Co)/ Al_2O_3 .

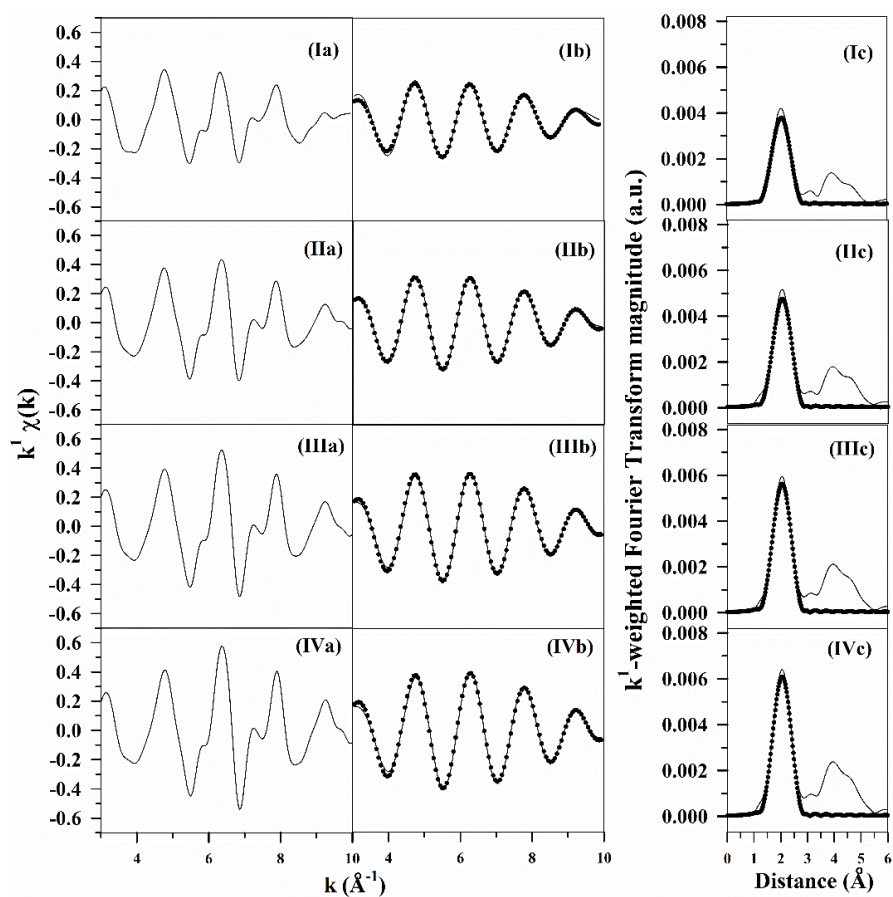


Figure 19. EXAFS fittings for Ni K-edge data, including (a) raw k^1 -weighted (k) data; (b) (solid line) filtered k^1 -weighted (k) data and (filled circles) results of the fittings; (c) (solid line) raw k^1 -weighted Fourier transform magnitude and (solid line) filtered k^1 -weighted Fourier transform magnitude; and (filled circles) results of the fittings for (I) 25%M ($M = 5\%Ni-95\%Co$)/ Al_2O_3 , (II) 25%M ($M = 10\%Ni-90\%Co$)/ Al_2O_3 , (III) 25%M ($M = 25\%Ni-75\%Co$)/ Al_2O_3 , and (IV) 25%M ($M = 50\%Ni-50\%Co$)/ Al_2O_3 .

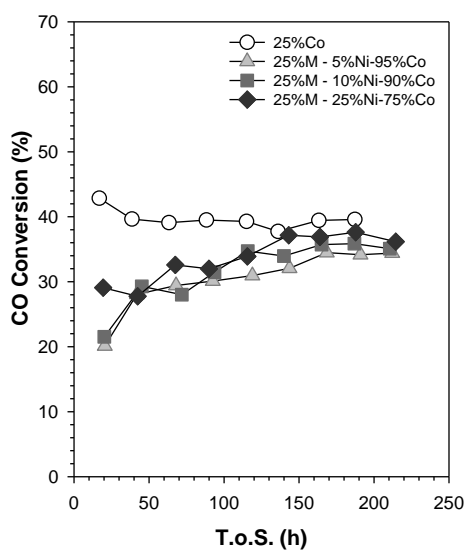


Figure 20. Evolution with T.o.S. of CO conversion for the prepared catalysts (process conditions: $T = 220$, $H_2/CO = 2$ mol/mol, $P = 20.6$ bar, $S.V. = 3.4$ slph per g_{cat}).

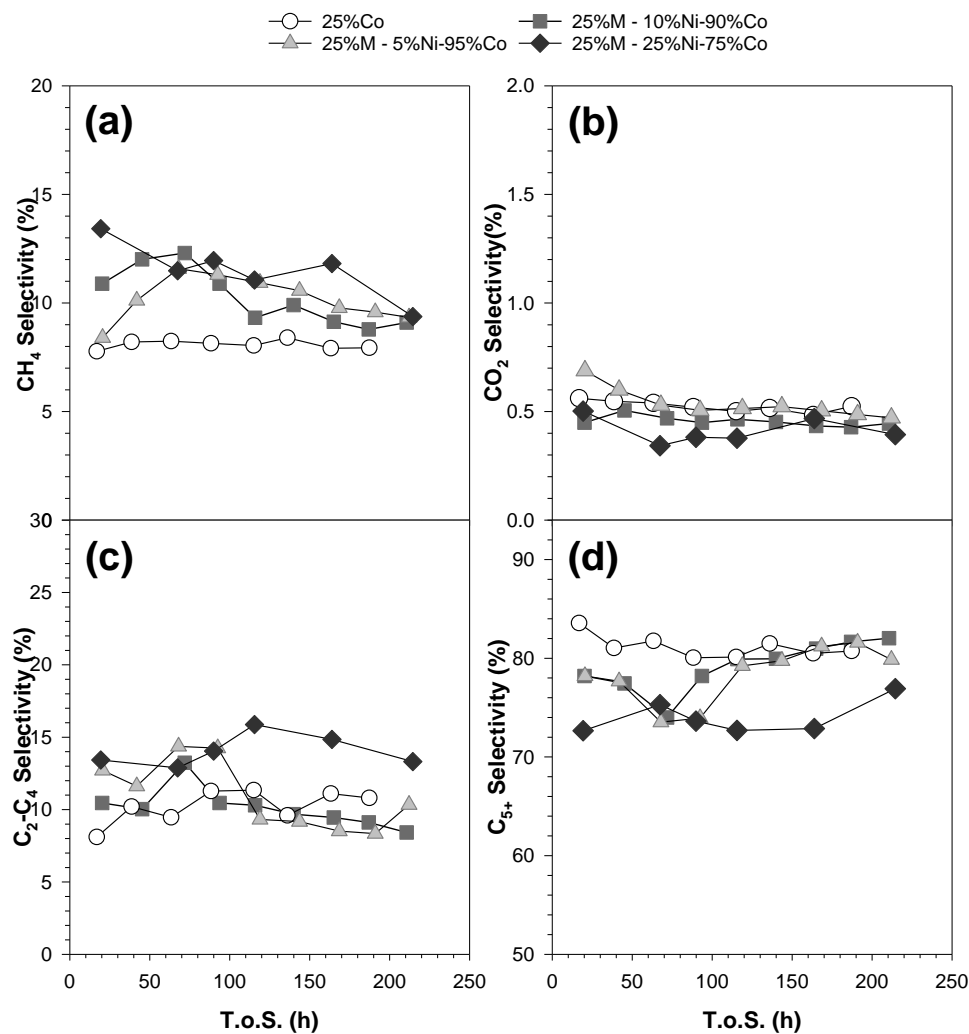


Figure 21. Evolution with T.o.S. of (a) CH₄, (b) CO₂, (c) C₂-C₄, (d) and C₅+ selectivities for the prepared catalysts (process conditions: P = 20.6 bar, H₂/CO = 2 mol/mol, T = 220 °C, S.V. = 3.4 slph per g_{cat}).

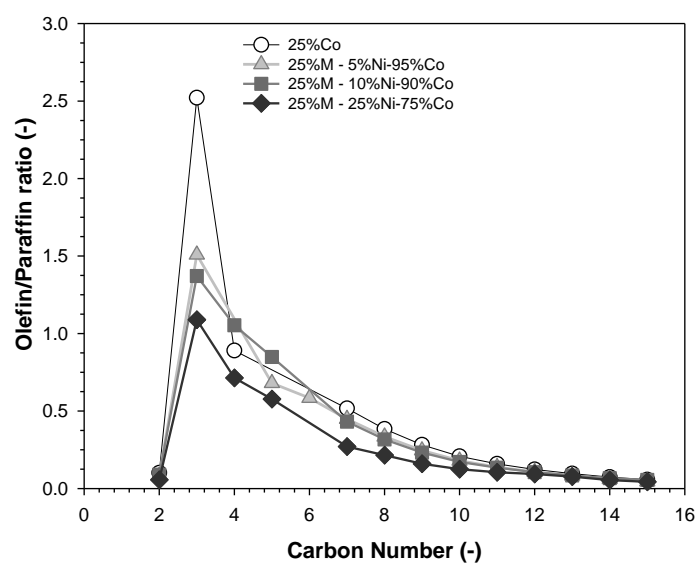


Figure 22. Olefin/paraffin ratio at T.o.S. ≈ 150 h (process conditions: P = 20.6 bar, H₂/CO = 2 mol/mol, T = 220 °C, S.V. = 3.4 slph per g_{cat}).

3. Discussion

The promotion of nickel on a cobalt-based catalyst does not significantly influence the morphological properties, as all the samples have similar surface areas ($\approx 92 \text{ m}^2/\text{g}$), pore volumes, and pore diameters. The effects of nickel on the structural properties were investigated by XRD and STEM. XRD patterns for all the calcined catalysts showed the typical peaks associated with Co_3O_4 , and no diffraction peaks associated with NiO or Ni^0 were observed, suggesting that a mixed metal oxide was formed. Intimate contact between cobalt and nickel was also confirmed by elemental mapping during STEM analysis, as well as by comparing TPR-XANES profiles at nickel and cobalt K-edges. Initially, nickel is associated with Co_3O_4 , and then it undergoes a change in the electronic structure to a form of nickel associated with CoO . Further evidence for solid solution formation is that the Ni^{2+} associated with Co_3O_4 (Ni K-edge results) and the Co_3O_4 reduce over a similar temperature range, such that the temperatures at 50% conversion match very well, especially at higher Ni/Co ratios.

TPR-XANES and hydrogen chemisorption/ O_2 titration show that nickel has a beneficial effect on cobalt reducibility. The reduction of cobalt oxide is shifted to a lower temperature with increasing Ni/Co ratio, and the percentage of metal reduction is increased. Voss et al. [19] observed an improvement in the reducibility when nickel was added, as the first reduction step shifted to a significantly lower temperature with increasing the nickel loading. The authors proposed a hydrogen spillover effect from the nickel sites to cobalt oxide sites. In the current work, the similarities in temperatures ranges between Co_3O_4 to CoO and $\text{Ni}^{2+}\text{-Co}_3\text{O}_4$ to $\text{Ni}^{2+}\text{-CoO}$, as well as similarities in the second reduction step from CoO to Co^0 and NiO to Ni^0 during TPR-XANES, suggest that in addition to H_2 spillover, a chemical promoting effect exists in leading to the formation of the Co-Ni alloy.

Cobalt-based catalysts are typically characterized by an initial decline and leveling off that occurs within the first few days. Possible mechanisms proposed for deactivation include: reoxidation of small metallic cobalt cluster to inactive CoO_x ; sintering; some carbon deposition or solid-state reaction between cobalt and the support [4,25,26]. Thermodynamic calculations show that when the cobalt crystallites have a diameter lower than 4.4 nm, they may be reoxidized in the steam/hydrogen environments of FTS [7,8], but this may occur rapidly before the first measurement is taken. The initial decline and leveling off period for CO conversion typical of cobalt-based catalysts was not observed for the nickel promoted catalysts. Rytter et al. [18] have also observed an activation period in the first 40 h. They proposed a catalyst reconstruction in the first stage of operation where nickel and cobalt partially segregate, thereby exposing the cobalt clusters to FTS reaction. However, additional investigations are needed to speculate the events occurring during this induction time. Interestingly, the performances of nickel-promoted catalysts are stable, despite having lower cobalt loading than 25%Co/ Al_2O_3 . This suggests that nickel can stabilize cobalt metal nanoparticles. Rytter et al. [18] further proposed that the higher stability for Co-Ni alloys could be due to a suppression in carbon deposition and a suppression of reoxidation phenomena via H_2 spillover.

The addition of nickel changed the product distribution. In particular, the initial methane selectivity increases by increasing the nickel loading, whereas the initial C_{5+} selectivity decreases. Higher CH_4 selectivities were also observed in previous works, where different Ni/Co ratios were studied [10,16,18]. Interestingly, the selectivities of Co/Ni catalysts improve with time on-stream to nearly match those of pure Co catalysts. Furthermore, the olefin content decreases, as does the chain growth probability with increasing Ni/Co ratio. These results are not surprising because of the high hydrogenation capability of nickel. Furthermore, Ishihara et al. [12] studied Co-Ni alloys supported on SiO_2 and found that cobalt electronically interacts with nickel in the outer shell orbitals by creating adsorption sites possessing a new electron density. These new sites have the highest H adsorption strengths. Thus, hydrogen competes more effectively for adsorption sites during co-adsorption of CO and H_2 with Co-Ni alloys relative to the pure cobalt based catalyst.

Finally, it is interesting to compare the activity/\$ (Table 4), as nickel and cobalt have different market prices. The price of cobalt is reported to be 2.13 times the price of nickel. Thus, the partial substitution of cobalt with nickel would be an advantage in terms of total catalyst cost. At steady

state conditions, the activity/\$ for the 25%M—25%Ni-75%Co is best for both the nickel-promoted and unpromoted catalyst; additionally, at that point, the selectivities of the CoNi catalysts nearly match those of the pure Co based catalyst.

Table 4. Activity/\$ at steady-state conditions for the tested catalysts.

Sample ID	Activity/\$
25%Co	39.5
25%M—5%Ni-95%Co	35.4
25%M—10%Ni-90%Co	36.8
25%M—25%Ni-75%Co	41.9

4. Materials and Methods

4.1. Catalyst Preparation

The conventional slurry impregnation method was used to prepare the catalyst containing 25% metal by weight, with the following Ni/Co atomic ratios: 0/100, 5/95, 10/90, 25/75, and 50/50. The support was Catalox 150 γ -alumina with a surface area of 150 m²/g. Nickel nitrate and cobalt nitrate (Alfa Aesar) served as the precursors to load the nickel and cobalt together (i.e., in a single solution) onto the γ -Al₂O₃ support. In this method, the ratio of the weight of alumina to the volume of solution used was 1:1, as reported in a Sasol patent [1], such that the loading solution prepared was approximately 2.5 times that of the pore volume. The total metal loading was added by two impregnation steps with 12.5% of metal by weight for each step. Between each step, the catalyst was dried at 60 °C under vacuum in a rotary evaporator; then, the temperature was slowly increased until 100 °C. After the second impregnation, the catalyst was dried and then calcined in flowing air for 4 h at 350 °C.

4.2. Characterization

A Micromeritics 3-Flex system (Norcross, GA, USA) using N₂ (UHP N₂, Airgas, Lexington, KY, USA) for physisorption was used to measure BET surface area and porosity properties. Before testing, the samples were pretreated at 160 °C and 50 mTorr for at least 12 h. The BJH method was employed to calculate the average pore volume and pore diameter.

XRD spectra were collected with a Philips X'Pert diffractometer (Amsterdam, The Netherlands) with monochromatic Cu K α radiation ($\lambda = 1.54\text{\AA}$). The conditions employed included a scan rate of 0.01° per step, 2 θ range of 10–90, and scan time of 4 s per step.

Prior to STEM characterization, the samples were pretreated in hydrogen (American Welding and Gas, Lexington, KY, USA) at 350 °C for 18 h, cooled down to room temperature, and then passivated with a mixture of 1% O₂ in nitrogen (American Welding and Gas, Lexington, KY, USA). STEM analysis was performed with an FEI Talos F200X instrument (Thermo Scientific, Waltham, MA, USA) equipped with BF, DF2, DF4, and HAADF detectors. The imaging was collected with a field emission gun using an accelerating voltage of 200 kV and a high speed Ceta 16M camera; Velox software (Thermo Scientific, Waltham, MA, USA) was used for data processing. The samples were dispersed in ethanol (Alfa Aesar, Haverhill, MA, USA), sonicated, and then dropped onto a carbon-coated copper grid and dried in air.

Hydrogen chemisorption and the ensuing pulse reoxidation were carried out using an Altamira AMI-300 unit (Altamira Instruments, Pittsburgh, PA, USA). The sample was reduced at 350 °C (ramping rate at 2 °C/min) for 10 h in 10 cm³/min of UHP H₂ (Airgas, San Antonio, TX, USA) blended with 20 cm³/min of UHP argon (Airgas, San Antonio, TX, USA). Then, the temperature was cooled to 100 °C, and UHP argon (30 cm³/min) was flowed through the catalytic bed to avoid the adsorption of weakly bound hydrogen. Next, the temperature was increased to 350 °C at 10 °C/min in flowing argon to desorb the chemisorbed hydrogen. The hydrogen peak obtained during the temperature programmed desorption was integrated and the moles of hydrogen evolved was determined by comparing to calibration pulses. Pulses of UHP O₂ (Airgas, San Antonio, TX, USA) were then passed through

the reactor to reoxidize the catalyst until saturation was achieved. The percentage of reduction was estimated with two different methods. In the first approach, nickel and cobalt metal were assumed to oxidize to NiO and Co₃O₄, respectively. However, in a second approach, we assumed all Co₃O₄ converted at least to CoO during the reduction, and that a fraction of NiO and CoO converted to Ni⁰ and Co⁰. Thus, during the reoxidation step, the Ni⁰ and Co⁰ are first oxidized to NiO and CoO. Then, all CoO oxidizes to Co₃O₄. These two approaches set minimum and maximum limits for the cobalt cluster size when the uncorrected dispersion is modified by considering the percentage of reduction by the metal, as follows:

% Dispersion (uncorrected) = (# metal atoms on the surface)/(# metal atoms in the sample)

% Disp. (corrected) = (# metal atoms on the surface)/((# metal atoms in the sample)(% reduction))

4.3. H₂-TPR XANES-EXAFS

In-situ H₂-TPR XAFS experiments were carried out at the Materials Research Collaborative Access Team (MR-CAT) beamline at the Advanced Photon Source, Argonne National Laboratory. A cryogenically cooled Si (1 1 1) monochromator selected the incident energy and a rhodium-coated mirror rejected higher order harmonics of the fundamental beam energy. The experiment setup was analogous to that outlined by Jacoby [27]. The in-situ TPR of 6 catalysts were performed in stainless-steel multi-sample holder (3.0 mm i.d. channels). Approximately 6 mg of each catalyst was loaded as a self-supporting wafer in each channel. The catalyst was diluted with alumina in a weight ratio of approximately 1:1. The holder was located in the center of a quartz tube and equipped with Kapton windows, a thermocouple, and gas ports. The amount of catalyst loaded was optimized for the Co and Ni K edges, considering the absorption by aluminum of the Al₂O₃. The quartz tube was positioned in a clamshell furnace mounted on the positioning table. Each sample cell was placed relative to the beam, and the position of the table was adjusted to an accuracy of 20 μm (for repeated scans). Once the catalyst positions were fine-tuned, the reactor was purged with He (100 mL/min) for more than 5 min, and then the reactant gas (a mixture H₂/He, 3.5%) was flowed through the samples (100 mL/min). The temperature was increased to 700 °C (ramp of ≈ 1.0 °C/min) and then held for 4 h. The Ni and Co K-edge spectra were collected in transmission mode. The Co metallic foil spectrum was also recorded simultaneously for energy calibration. X-ray absorption spectra for each catalyst were collected from 7500 to 9000 eV.

The WinXAS program was used to analyze the spectra collected during H₂-TPR EXAFS/XANES experiments [28]. Additional details of the EXAFS and XANES analyses for Co K-edge data are reported in our previous work [29]. Ni K-edge data were processed in a similar manner (i.e., same Δk and ΔR in fittings). For qualitative comparisons of EXAFS and XANES results, the references used for Co⁰, CoO, and Co₃O₄ were the final spectrum, the point of maximum CoO content, and the initial spectrum of the TPR trajectory of undoped cobalt catalyst (25%Co/Al₂O₃). For Ni⁰ and NiO, the references were NiO (Alfa Aesar, Puratronic, 99.998%, Tewksbury, MA, USA) and a Ni⁰ foil.

For XANES analyses, linear combination fittings were carried out considering as reference compounds for Co K-edge data, the initial spectrum (a mixture of Co³⁺ and Co²⁺ similar to Co₃O₄), the point of maximum CoO content, and the final spectrum after H₂ TPR (representing Co⁰). At the Ni K-edge, the reference compounds were the first spectrum (Ni²⁺ associated with Co₃O₄), the spectrum with highest CoO content, where Ni²⁺ is associated with the CoO, and the final spectrum after H₂ TPR (representing ≈ 100% Ni⁰). The data reduction and fitting for EXAFS were performed using the catalysts in their final state following TPR and cooling in flowing H₂ using the WinXAS [28], Atoms [30], FEFFIT [31], and FEFF [31] programs. The k-range chosen for the fittings was 3–10 Å⁻¹. Fitting was confined to the first metallic coordination shell by applying a Hanning window in the Fourier transform magnitude spectra, and carrying out the back-transform to isolate that shell.

4.4. Reaction Testing

Activity tests were performed using a 1 L continuously stirred tank reactor (CSTR) (PPI, Warminster, PA, USA). Additional information on the laboratory-scale rig can be found elsewhere [32]. In a typical test, 9.6 g of catalyst ($63 < dp < 125 \mu\text{m}$) were loaded into a fixed bed reactor. The catalyst was reduced at $350 \text{ }^\circ\text{C}$ for 20 h, while being fed a 30 NL/h H_2/He mixture (1:3 v/v, American Welding and Gas, Lexington, KY, USA) at atmospheric pressure. The reduced catalyst was transferred by pneumatic transfer under the protection of inert gas to a CSTR containing 310 g of melted Polywax 3000 (Baker Petrolite, Houston, TX, USA). In-situ reduction of the transferred catalyst was performed at atmospheric pressure and $230 \text{ }^\circ\text{C}$ with overnight feeding of 30 NL/h pure H_2 (American Welding and Gas, Lexington, KY, USA). In this work, the catalytic testing was carried out at the following process conditions: $P = 20.2 \text{ bar}$, $T = 220 \text{ }^\circ\text{C}$, a stirring speed of 750 rpm, and $\text{H}_2/\text{CO} = 2 \text{ mol/mol}$. The unconverted reactants and the products leaving the CSTR were sent to a warm trap, in which the temperature was set at $100 \text{ }^\circ\text{C}$, and then to a cold trap maintained at $0 \text{ }^\circ\text{C}$. The uncondensed stream was reduced to atmospheric pressure, while the flowrate and the composition were measured by a wet test meter and by an online 3000A micro-GC (Agilent, Santa Clara, CA, USA), respectively. The micro-GC is equipped with four different columns (Plot U, Molecular Sieve, OV-1 and, Alumina) and TCD. The reaction products were collected in three traps maintained at different temperatures: a hot trap ($200 \text{ }^\circ\text{C}$), a warm trap ($100 \text{ }^\circ\text{C}$), and a cold trap ($0 \text{ }^\circ\text{C}$). The products were separated into different fractions (wax, oil, and aqueous) for quantification. The oil ($\text{C}_4\text{--C}_{20}$) fraction was analyzed with a 7890 GC (Agilent, Santa Clara, CA, USA) equipped with DB-5 ($60 \text{ m} \times 0.32 \text{ mm} \times 0.25 \mu\text{m}$, Agilent J&W) column and FID, whereas waxes ($\text{C}_{21}\text{--C}_{60}$) were analyzed with an HP 6890 GC equipped with ZB-1HT column ($30 \text{ m} \times 0.25 \text{ mm} \times 0.10 \mu\text{m}$, Zebron) and FID.

5. Conclusions

Bimetallic catalysts with different Ni/Co ratios were prepared by standard aqueous incipient impregnation. N_2 adsorption/desorption results show that the addition of nickel had no effect on the morphological properties, as similar surface areas, pore volumes, and pore diameters were obtained independently from the Ni/Co ratio. XRD patterns of the samples exhibited peaks associated with Co_3O_4 , whereas no diffraction peaks associated with Ni were observed. Thus, this suggests a Co–Ni solid oxide solution might be formed. STEM and TPR-XANES show the nickel and cobalt are in intimate contact, strongly suggesting the formation of a Co–Ni alloy from a Co oxide – Ni oxide solid solution. Moreover, TPR-XANES results indicate that nickel promotion improves the cobalt reducibility by systematically shifting the reduction profiles to lower temperatures. The similarities in temperature ranges between Co_3O_4 to CoO and $\text{Ni}^{2+}\text{--Co}_3\text{O}_4$ to $\text{Ni}^{2+}\text{--CoO}$, and the second reduction step to the metallic phase (i.e., CoO to Co^0 and NiO to Ni^0) during TPR-XANES, suggest that not only is H_2 spillover involved, but a chemical effect is likely. This is due to intimate contact of Co and Ni in the solid solution that leads to the formation of the Co–Ni alloy.

The catalyst's performance during FTS, in terms of conversion, selectivity, and stability, was evaluated using a CSTR. Nickel-promoted catalysts have lower initial CO conversion, which progressively increases with T.o.S. until a steady-state value is achieved. This CO conversion trend is inverted compared to the typical induction period observed for $\text{Co}/\text{Al}_2\text{O}_3$, where the activity progressively declines and levels off because of deactivation phenomena. The stability of the Co–Ni alloy may be due to the stabilization of metallic cobalt nanoparticles by nickel addition, resulting in robust nanoparticles even at lower cobalt content compared to commercial Co loadings. CH_4 selectivity increases by increasing nickel loading because of the higher hydrogenation capability of the Co–Ni alloy. However, the difference in CH_4 selectivity between the Ni-promoted and unpromoted catalyst (in terms of the absolute value) decreases with T.o.S., which is beneficial; in fact, after stabilization, the C_5+ selectivities were quite similar between catalysts prepared with Co–Ni bimetallic mixtures and Co alone. Finally, the steady-state activity/\$ for a Ni/Co ratio of 25/75 is slightly higher than that of 25%Co/ Al_2O_3 .

Author Contributions: Conceptualization, catalyst preparation, catalyst characterization, formal analysis, writing, G.J. Catalyst preparation, catalyst characterization, formal analysis, S.C.K. Catalyst preparation, catalyst characterization, formal analysis, R.G. Catalyst preparation, catalyst characterization, formal analysis. C.D.W. Reaction testing, characterization, formal analysis, conceptualization, writing, M.M. Project administration, resources, C.L.M. Catalyst preparation, supervision, resources, D.C.C. Catalyst characterization, data curation, resources, supervision, A.J.K. Formal analysis W.D.S. All authors have read and agreed to the published version of the manuscript.

Funding: Richard Garcia received funding from a UTSA College of Engineering Scholarship. His work was also supported by the USDA National Institute of Food and Agriculture, Interdisciplinary Hands-on Research Traineeship and Extension Experiential Learning in Bioenergy/Natural Resources/Economics/Rural project, U-GREAT (Undergraduate Research, Education and Training) program (2016-67032-24984). Caleb D. Watson acknowledges support from the Undergraduate NSF Research Program, supported by the National Science Foundation through grant award #1832388.

Acknowledgments: Argonne's research was supported in part by the U.S. Department of Energy (DOE), Office of Fossil Energy, National Energy Technology Laboratory (NETL). Advanced photon source was supported by the U.S. Department of Energy, Office of Science, Office of Basic Energy Sciences, under contract number DE-AC02-06CH11357. MRCAT operations are supported by the Department of Energy and the MRCAT member institutions. CAER research was supported by the Commonwealth of Kentucky. Richard Garcia would like to acknowledge funding from a UTSA College of Engineering Scholarship. His work was also supported by the USDA National Institute of Food and Agriculture, Interdisciplinary Hands-on Research Traineeship, and Extension Experiential Learning in Bioenergy/Natural Resources/Economics/Rural project, U-GREAT (Undergraduate Research, Education and Training) program (2016-67032-24984). Caleb D. Watson would like to acknowledge support from the Undergraduate NSF Research Program, supported by the National Science Foundation through grant award #1832388. Gary Jacobs would like to thank UTSA and the State of Texas for financial support through startup funds.

Conflicts of Interest: The authors declare no conflict of interest.

References

1. Schulz, H. Short history and present trends of Fischer–Tropsch synthesis. *Appl. Catal. A Gen.* **1999**, *186*, 3–12. [[CrossRef](#)]
2. Shafer, W.D.; Gnanamani, M.K.; Graham, U.M.; Yang, J.; Masuku, C.M.; Jacobs, G.; Davis, B.H. Fischer–Tropsch: Product selectivity—The fingerprint of synthetic fuels. *Catalysts* **2019**, *9*, 259. [[CrossRef](#)]
3. Khodakov, A.Y.; Chu, W.; Fongarland, P. Advances in the development of novel cobalt Fischer–Tropsch catalysts for synthesis of long-chain hydrocarbons and clean fuels. *Chem. Rev.* **2007**, *107*, 1692–1744. [[CrossRef](#)] [[PubMed](#)]
4. Jahangiri, H.; Bennett, J.; Mahjoubi, P.; Wilson, K.; Gu, S. A review of advanced catalyst development for Fischer–Tropsch synthesis of hydrocarbons from biomass derived syn-gas. *Catal. Sci. Technol.* **2014**, *4*, 2210–2229. [[CrossRef](#)]
5. Glacier, I. Resource Management Group. Available online: <http://www.infomine.com/investment> (accessed on 20 December 2019).
6. Iglesia, E. Design, synthesis, and use of cobalt-based Fischer–Tropsch synthesis catalysts. *Appl. Catal. A Gen.* **1997**, *161*, 59–78. [[CrossRef](#)]
7. Hou, C.; Xia, G.; Sun, X.; Wu, Y.; Jin, C.; Yan, Z.; Li, M.; Hu, Z.; Nie, H.; Li, D. Thermodynamics of oxidation of an alumina-supported cobalt catalyst by water in F-T synthesis. *Catal. Today* **2016**, *264*, 91–97. [[CrossRef](#)]
8. Van Steen, E.; Claeys, M.; Dry, M.E.; Van de Loosdrecht, J.; Viljoen, E.L.; Visagie, J.L. Stability of nanocrystals: Thermodynamic analysis of oxidation and re-reduction of cobalt in water/hydrogen mixtures. *J. Phys. Chem. B* **2005**, *109*, 3575–3577. [[CrossRef](#)]
9. Jacobs, G.; Patterson, P.M.; Das, T.K.; Luo, M.; Davis, B.H. Fischer–Tropsch synthesis: Effect of water on Co/Al₂O₃ catalysts and XAFS characterization of reoxidation phenomena. *Appl. Catal. A Gen.* **2004**, *270*, 65–76. [[CrossRef](#)]
10. Van Helden, P.; Prinsloo, F.; Van den Berg, J.-A.; Xaba, B.; Erasmus, W.; Claeys, M.; Van de Loosdrecht, J. Cobalt-nickel bimetallic Fischer–Tropsch catalysts: A combined theoretical and experimental approach. *Catal. Today* **2020**, *342*, 88–98. [[CrossRef](#)]
11. Shadravan, V.; Bukas, V.J.; Gunasooriya, G.T.K.K.; Waleson, J.; Drewery, M.; Karibika, J.; Jones, J.; Kennedy, E.; Adesina, A.; Nørskov, J.K.; et al. Effect of manganese on the selective catalytic hydrogenation of CO_x in the presence of light hydrocarbons over Ni/Al₂O₃: An experimental and computational study. *ACS Catal.* **2020**, *10*, 1535–1547. [[CrossRef](#)]

12. Ishihara, T.; Horiuchi, N.; Inoue, T.; Eguchi, K.; Takita, Y.; Arai, H. Effect of alloying on CO hydrogenation activity over SiO₂-supported Co-Ni alloy catalysts. *J. Catal.* **1992**, *136*, 232–241. [[CrossRef](#)]
13. Ishihara, T.; Iwakuni, H.; Eguchi, K.; Arai, H. Hydrogenation of carbon monoxide over the mixed catalysts composed of cobalt-nickel/manganese oxide-zirconium oxide and zeolite catalysts. *Appl. Catal.* **1991**, *75*, 225–235. [[CrossRef](#)]
14. Ishihara, T.; Eguchi, K.; Arai, H. Hydrogenation of carbon monoxide over SiO₂-supported Fe-Co, Co-Ni and Ni-Fe bimetallic catalysts. *Appl. Catal.* **1987**, *30*, 225–238. [[CrossRef](#)]
15. Sun, Y.; Wei, J.; Zhang, J.P.; Yang, G. Optimization using response surface methodology and kinetic study of Fischer–Tropsch synthesis using SiO₂ supported bimetallic Co–Ni catalyst. *J. Nat. Gas Sci. Eng.* **2016**, *28*, 173–183. [[CrossRef](#)]
16. Shimura, K.; Miyazawa, T.; Hanaoka, T.; Hirata, S. Fischer–Tropsch synthesis over alumina supported bimetallic Co–Ni catalyst: Effect of impregnation sequence and solution. *J. Mol. Catal. A Chem.* **2015**, *407*, 15–24. [[CrossRef](#)]
17. Eshraghi, A.; Mirzaei, A.A.; Rahimi, R.; Atashi, H. Effect of Ni–Co morphology on kinetics for Fischer–Tropsch reaction in a fixed-bed reactor. *J. Taiwan Inst. Chem. Eng.* **2019**, *105*, 104–114. [[CrossRef](#)]
18. Rytter, E.; Skagseth, T.H.; Eri, S.; Sjøstad, A.O. Cobalt Fischer–Tropsch catalysts using nickel promoter as a rhenium substitute to suppress deactivation. *Ind. Eng. Chem. Res.* **2010**, *49*, 4140–4148. [[CrossRef](#)]
19. Voss, G.J.B.; Fløystad, J.B.; Voronov, A.; Rønning, M. The state of nickel as promotor in cobalt Fischer–Tropsch synthesis catalysts. *Top. Catal.* **2015**, *58*, 896–904. [[CrossRef](#)]
20. López-Tinoco, J.; Mendoza-Cruz, R.; Bazán-Díaz, L.; Karuturi, S.C.; Martinelli, M.; Cronauer, D.C.; Kropf, A.J.; Marshall, C.L.; Jacobs, G. The preparation and characterization of Co–Ni nanoparticles and the testing of a heterogenized Co–Ni/alumina catalyst for CO hydrogenation. *Catalysts* **2019**, *10*, 18. [[CrossRef](#)]
21. Nikparsa, P.; Mirzaei, A.A.; Rauch, R. Modification of Co/Al₂O₃ Fischer–Tropsch nanocatalysts by adding Ni: A kinetic approach. *Int. J. Chem. Kinet.* **2016**, *48*, 131–143. [[CrossRef](#)]
22. Yu, H.; Zhao, A.; Zhang, H.; Ying, W.; Fang, D. Bimetallic catalyst of Co and Ni for Fischer–Tropsch synthesis supported on alumina, energy sources. *Part A Recovery Util. Environ. Eff.* **2015**, *37*, 47–54.
23. Jacobs, G.; Ma, W.; Gao, P.; Todic, B.; Bhatelia, T.; Bukur, D.B.; Davis, B.H. The application of synchrotron methods in characterizing iron and cobalt Fischer–Tropsch synthesis catalysts. *Catal. Today* **2013**, *214*, 100–139. [[CrossRef](#)]
24. Van Der Laan, G.P.; Beenackers, A.A.C.M. Kinetics and selectivity of the Fischer–Tropsch synthesis: A literature review. *Catal. Rev.* **1999**, *41*, 255–318. [[CrossRef](#)]
25. Tsakoumis, N.E.; Rønning, M.; Borg, Ø.; Rytter, E.; Holmen, A. Deactivation of cobalt based Fischer–Tropsch catalysts: A review. *Catal. Today* **2010**, *154*, 162–182. [[CrossRef](#)]
26. Jacobs, G.; Patterson, P.M.; Zhang, Y.; Das, T.; Li, J.; Davis, B.H. Fischer–Tropsch synthesis: Deactivation of noble metal-promoted Co/Al₂O₃ catalysts. *Appl. Catal. A Gen.* **2002**, *233*, 215–226. [[CrossRef](#)]
27. Jacoby, M. X-ray absorption spectroscopy. *Chem. Eng. News Arch.* **2001**, *79*, 33–38. [[CrossRef](#)]
28. Ressler, T. WinXAS: A program for X-ray absorption spectroscopy data analysis under MS-Windows. *J. Synchrotron Radiat.* **1998**, *5*, 118–122. [[CrossRef](#)]
29. Jacobs, G.; Ji, Y.; Davis, B.H.; Cronauer, D.; Kropf, A.J.; Marshall, C.L. Fischer–Tropsch synthesis: Temperature programmed EXAFS/XANES investigation of the influence of support type, cobalt loading, and noble metal promoter addition to the reduction behavior of cobalt oxide particles. *Appl. Catal. A Gen.* **2007**, *333*, 177–191. [[CrossRef](#)]
30. Ravel, B. ATOMS: Crystallography for the X-ray absorption spectroscopist. *J. Synchrotron Radiat.* **2001**, *8*, 314–316. [[CrossRef](#)]
31. Newville, M.; Ravel, B.; Haskel, D.; Rehr, J.J.; Stern, E.A.; Yacoby, Y. Analysis of multiple-scattering XAFS data using theoretical standards. *Phys. B Condens. Matter* **1995**, *208–209*, 154–156. [[CrossRef](#)]
32. Jacobs, G.; Ribeiro, M.C.; Ma, W.; Ji, Y.; Khalid, S.; Sumodjo, P.T.A.; Davis, B.H. Group 11 (Cu, Ag, Au) promotion of 15%Co/Al₂O₃ Fischer–Tropsch synthesis catalysts. *Appl. Catal. A Gen.* **2009**, *361*, 137–151. [[CrossRef](#)]

